

THESIS FOR THE DEGREE OF DOCTOR OF PHILOSOPHY
IN
THERMO AND FLUID DYNAMICS

Turbulence-resolving simulations for engineering applications

by

BASTIAN NEBENFÜHR

Department of Applied Mechanics
Division of Fluid Dynamics
CHALMERS UNIVERSITY OF TECHNOLOGY
Gothenburg, Sweden 2015

Turbulence-resolving simulations for engineering applications
BASTIAN NEBENFÜHR
ISBN 978-91-7597-254-1

© BASTIAN NEBENFÜHR, 2015

Doktorsavhandlingar vid Chalmers tekniska högskola
Ny serie nr. 3935
ISSN 0346-718X

Department of Applied Mechanics
Division of Fluid Dynamics
Chalmers University of Technology
SE-412 96 Gothenburg
Sweden
Telephone: +46 (0)31-772 1000

Cover:

Left panel: Instantaneous flow structures in the slat cove of the three-element airfoil.
Right panel: Instantaneous flow structures above a forest. Note that the wind turbines are not part of the simulation and were added later for illustrative purposes.

This document was typeset using \LaTeX

Printed at Chalmers Reproservice
Gothenburg, Sweden 2015

Turbulence-resolving simulations for engineering applications

BASTIAN NEBENFÜHR

Department of Applied Mechanics
Division of Fluid Dynamics
Chalmers University of Technology

ABSTRACT

Most fluid flows of industrial interest are turbulent and their accurate representation may be of vital importance for the design process of new products. To date, steady RANS methods are usually employed for the simulation of turbulent flows of everyday engineering problems. These methods base the description of turbulence characteristics on mean-flow gradients and only provide a solution for the mean flow. However, there are applications that require instantaneous flow information, for which the use of unsteady, turbulence-resolving simulation techniques is indispensable. In this thesis, the latter have been applied to predict two flow problems of industrial importance. Additionally to providing the flow solution, the simulation method's capability of producing input data for subsequent multi-disciplinary analysis was evaluated.

In the first case, hybrid RANS/LES methods were used for simulating the complex flow around a three-element airfoil with deployed high-lift devices. Instantaneous flow properties were extracted from the simulation via a sampling surface and served as input for a subsequent aeroacoustic analysis of the airfoil using acoustic analogies. It was found that the chosen hybrid RANS/LES simulation technique was well-suited for computing the flow. Moreover, decoupling the flow simulation and the noise propagation enables aeroacoustic analysis and farfield-noise prediction for complex geometries at relevant Reynolds numbers. The slat was confirmed to be a major contributor to high-lift noise. Careful placement of the sampling surface, so as to enclose all turbulent noise sources, seems to be of paramount importance, in particular for using the Kirchhoff analogy.

The second case dealt with LES simulations of the atmospheric boundary layer above and inside forest regions. Also from these simulations, instantaneous turbulence data were extracted, serving as inflow data in subsequent fatigue-load calculations for a wind turbine. It was expected that the presence of a forest would lead to stronger atmospheric turbulence and increased wind shear, compared to flow over low-roughness flat terrain. By simulating the atmospheric boundary layer with and without a forest, this expectation could be verified and it was possible to quantify the effect of the forest on the wind-turbine fatigue loads. It could be shown that typical loads are increased by a factor of almost three in terms of root-mean-square values and equivalent fatigue loads.

Keywords: Turbulence-resolving simulation, LES, hybrid RANS/LES, Airframe noise, Aeroacoustics, Wind power, Wind-turbine fatigue loads, Forest canopy

ACKNOWLEDGEMENTS

First and foremost, I want to express my gratitude to my advisor, Lars Davidson, who gave me the opportunity to carry out this work. Lars, your constant support, positive attitude and helpful discussions were crucial ingredients for success during the last five years.

I am also grateful to Shia-Hui Peng for introducing me to the Edge solver and for always being eager to discuss my results with me and to provide inspiration for further work. Thank you, Lars-Erik Eriksson and Huadong Yao, for introducing me to the world of aeroacoustics and your patience. I also want to thank Ingemar Carlén for interesting discussions about wind power and atmospheric turbulence.

Special thanks go to Luca Caracaglia for making my stay at Northeastern University possible. Thank you for always keeping an open door for me, despite your busy schedule. I would like to thank Ulla and Monica for all the help and for keeping this department rolling.

Thank you, Matthias, Pirooz and Anke for proofreading this thesis.

I am grateful to all my previous and present colleagues at the division of fluid dynamics, who contributed to a pleasant working atmosphere. In particular, I want to mention in this regard my office mates Pirooz, Guillaume, Marcus and Alexandre. Thank you, Martin for countless coffee breaks and your tireless efforts to teach me Swedish culture. A big shout-out to the climbing family, in particular Peter, Johanna, Mirko and Haukur! Thanks for always offering a welcome distraction from sitting in front of a computer screen.

I am extremely grateful to my family, who always kept supporting me, even when my initial 11-month-stay in Sweden turned into 7 years!

Last, but not least, I want to thank my loving girlfriend Anke for her constant support and encouragement.

The financial support of SNIC (the Swedish National Infrastructure for Computing) for computer time at C3SE (Chalmers Center for Computational Science and Engineering) is gratefully acknowledged. Furthermore, computer time at PDC (Center for High Performance Computing) at KTH Stockholm is acknowledged.

Part of this work was financed by the EU project ATAAC (Advanced Turbulence Simulation for Aerodynamic Application Challenges), Grant Agreement No. 233710. Further information about the ATAAC project is provided at <http://cfm.mace.manchester.ac.uk/ATAAC/WebHome>.

Part of this work was financed through the Swedish Wind Power Technology Centre (SWPTC). SWPTC is a research centre for the design of wind turbines. The purpose of the centre is to support Swedish industry with knowledge of design techniques as well as maintenance in the field of wind power. The Centre is funded by the Swedish Energy Agency, Chalmers University of Technology as well as academic and industrial partners.

LIST OF PUBLICATIONS

This thesis consists of an extended summary and six appended papers. Papers A–D are published in peer-reviewed conference proceedings, while Paper E is published in a scientific journal. Paper F is currently under review for journal publication.

- Paper A** B. Nebenführ, S.-H. Peng, and L. Davidson. “Hybrid RANS-LES Simulation of Turbulent High-Lift Flow in Relation to Noise Generation”. *Progress in Hybrid RANS-LES Modelling, NNFM*. ed. by S. Fu et al. Vol. 117. Springer, 2012, pp. 303–314
- Paper B** B. Nebenführ, H. Yao, S.-H. Peng, and L. Davidson. “Hybrid RANS/LES Simulations for Aerodynamic and Aeroacoustic Analysis of a Multi-Element Airfoil”. *19th AIAA/CEAS Aeroacoustics Conference*. AIAA paper 20013-2066. Berlin, Germany, 27–29 May, 2013
- Paper C** B. Nebenführ and L. Davidson. “Influence of a forest canopy on the neutral atmospheric boundary layer - A LES study”. *ETMM10: 10th International ERCOFTAC Symposium on Engineering Turbulence Modelling and Measurements*. Marbella, Spain, 17–19 September, 2014
- Paper D** B. Nebenführ, I. Carlén, L. Caracoglia, and L. Davidson. “Development of a reduced-order model for wind turbine response to atmospheric turbulence in forest regions”. *6th International Symposium on Computational Wind Engineering*. Hamburg, Germany, 8–12 June, 2014
- Paper E** B. Nebenführ and L. Davidson. Large-eddy simulation study of thermally stratified canopy flow. *Boundary-Layer Meteorology* **156.2** (2015), pp. 253–276. DOI: 10.1007/s10546-015-0025-9
- Paper F** B. Nebenführ and L. Davidson. Prediction of wind turbine fatigue loads in forest regions based on turbulent LES inflow fields. *submitted to Wind Energy* (2015)

DIVISION OF WORK

All papers were written by B. Nebenführ, who also performed all numerical simulations. In Papers A and B, S.-H. Peng provided guidance and helpful discussions. H. Yao provided the software for the aeroacoustic calculations presented in Paper B and helped with interpretation of results. The reduced-order model in Paper D was developed and implemented during B. Nebenführ's extended visit to Northeastern University in Boston, MA. L. Caracoglia contributed with discussions about structural dynamics and helped implementing the reduced-order model. Load calculations with ViDyn presented in Paper D were performed by I. Carlén from Teknikgruppen. L. Davidson was the main supervisor and provided guidance and helpful discussions, helped with interpretation of results and supplied the LES code used in Papers C–F. All fatigue load calculations using FAST were carried out by B. Nebenführ.

OTHER RELEVANT PUBLICATIONS

Other publications related to thesis:

- Publication I** S.-H. Peng, B. Nebenführ, and L. Davidson. “Lessons learned from hybrid RANS-LES computations of a three-element airfoil flow”. *21st AIAA Computational Fluid Dynamics Conference* San Diego, USA, 24–27 June, 2013

CONTENTS

Abstract	i
Acknowledgements	iii
List of publications	v
Contents	ix
I Extended Summary	1
1 Introduction	1
1.1 Turbulent flows	1
1.2 Boundary layers	2
1.2.1 The atmospheric boundary layer	4
1.3 Simulation of turbulent flows	5
2 Turbulence-resolving simulation techniques	9
2.1 Governing equations	9
2.2 The LES framework	10
2.3 Treatment of the near-wall region	12
2.3.1 LES with a wall function	12
2.3.2 Hybrid RANS/LES methods	13
2.4 Models used in this thesis	16
2.4.1 Deardorff's k -equation SGS model	16
2.4.2 DES based on the SA model (SADES)	17
2.4.3 An algebraic hybrid RANS/LES model (HYB0)	18
3 Applications	21
3.1 Aerodynamic and aeroacoustic analysis of a multi-element airfoil	21
3.1.1 Previous work	23
3.1.2 Simulations and work flow	24
3.1.3 Numerical description	26
3.1.4 Typical results	27
3.2 Wind-turbine fatigue loads in forest regions	28
3.2.1 Previous work	31
3.2.2 LES within and above a forest	31
3.2.3 Numerical description	35
3.2.4 Fatigue-load simulations	36
3.2.5 Typical results	37
4 Summary of papers	41
4.1 Paper A	41

4.1.1	Summary	41
4.1.2	Comments	41
4.2	Paper B	42
4.2.1	Summary	42
4.2.2	Comments	42
4.3	Paper C	43
4.3.1	Summary	43
4.3.2	Comments	43
4.4	Paper D	43
4.4.1	Summary	43
4.4.2	Comments	44
4.5	Paper E	44
4.5.1	Summary	44
4.5.2	Comments	45
4.6	Paper F	45
4.6.1	Summary	45
4.6.2	Comments	46
5	Concluding remarks	47
	References	49
A	Aeroacoustic analogies	61
A.1	Kirchhoff surface integral method	61
A.2	Ffowcs-Williams and Hawkings' analogy	62
A.3	Curle's analogy	63
II	Appended Papers A–F	65

Part I

Extended Summary

This thesis focuses on the application of turbulence-resolving simulation methods for the investigation of flow problems of industrial importance. It consists of an extended summary and six appended papers. Below, a brief introduction is given concerning turbulent flows, boundary layers and common simulation techniques for turbulent fluid flow. In Chapter 2, the governing equations are presented and the framework of turbulence-resolving simulations is detailed. Additionally, the specific techniques used in this thesis are described. Chapter 3 concerns the two different industrial applications that were treated during this work. Firstly, as a typical example of the aeronautic industry, the turbulent flow around a multi-element airfoil with deployed high-lift devices in landing configuration was investigated using hybrid RANS/LES methods (HRLM). In addition, the airfoil's aeroacoustic far-field noise signature was analyzed based on resolved turbulence extracted from the flow simulation. Secondly, as a typical example of meteorology and the wind-energy industry, the turbulence in the atmospheric boundary layer (ABL) and, in particular, in the ABL above forests, was investigated using Large-Eddy Simulation (LES) with a wall function. Additionally, resolved turbulence was extracted from the flow simulations, which was subsequently used as input for fatigue-load calculations on a generic wind turbine. In Chapter 4, the appended papers are summarized, followed by general concluding remarks in Chapter 5. In Part II of this thesis, the appended papers can be found.

1 Introduction

In the following, a short introduction in turbulent flows, boundary layers and common techniques for the simulation of turbulent flows will be given.

1.1 Turbulent flows

Fluid flows of engineering importance are almost exclusively turbulent. Even in our everyday life, there are many examples in which we encounter turbulence and turbulent flows. Illustrative examples include: the flow of water in a river; smoke rising from a fire, chimney or a cigarette; the airflow around a traveling vehicle (in Sweden often visualized by either rain or snowflakes); leaves being picked up and convected by the wind; and adding milk to a cup of coffee. There is no clear definition of turbulence itself, but people have observed some of its characteristics and often use them for its description. Obvious features include the swirling motions at different length and time scales and the irregular and seemingly random nature of turbulence that can be observed in the aforementioned examples. Turbulence is a phenomenon that is always unsteady and three dimensional. It may seem unpredictable, but turbulence can be described mathematically. Moreover, turbulence is known to increase diffusivity in a flow. In other words, turbulence increases

the flow's ability to mix, for example, momentum or heat (compared to laminar flows). This is an interesting effect that can be exploited for engineering purposes (i.e. cooling with forced convection or dispersion of pollutants in water or the atmosphere).

Probably the most important dimensionless quantity in turbulent flows is the Reynolds number,

$$Re = \frac{\rho UL}{\mu}, \quad (1.1)$$

where ρ and μ are the density and viscosity of the fluid and U and L are a velocity and a length scale characteristic for the flow, respectively. The Reynolds number can be interpreted as the ratio of inertial forces to viscous forces, meaning that, the higher the Reynolds number is, the more important inertial forces are, and vice versa. Often the distinction between turbulent and laminar flows is made based on the Reynolds number. Generally speaking, turbulent flows are characterized by high Reynolds numbers and are therefore dominated mainly by inertial forces. However, the critical Reynolds number, below which the flow can be viewed as laminar and above which the flow should be considered turbulent, depends on the choice of both U and L , and is thus dependent on the flow problem at hand. For example, the critical Reynolds number for a fully-developed pipe flow based on the pipe diameter and the bulk velocity is usually given as $Re_c = 2300$ [8].

One important characteristic of turbulent flows is that they are dissipative, meaning that they lose part of their energy (kinetic energy that is) to internal energy (i.e. increased temperature). This happens through the so-called cascade process, visualized in Fig.1.1. The large, energy-bearing eddies in region I extract kinetic energy from the mean flow and pass it on to subsequently smaller eddies. Energy transfer from larger to smaller eddies continues through the entire inertial subrange (region II) until the smallest eddies, the Kolmogorov scales, are reached in region III. Turbulent eddies in the third region are typically isotropic and dissipation occurs here, due to viscosity effects. Note that, since friction forces exist at all scales, a small portion of the kinetic energy is dissipated directly from the large eddies [9], but the major part of the kinetic energy is indeed undergoing the cascade process and is dissipated by the smallest eddies. As a consequence of the cascade process, turbulence needs a constant supply of additional kinetic energy (typically from the mean flow) to be sustained.

1.2 Boundary layers

Every time a fluid starts flowing over a solid surface, a boundary layer is formed. The boundary layer is the region of the flow that is influenced by surface forces, while the part of the flow uninfluenced by the surface forces is usually referred to as the freestream. At the interface between the solid wall and the fluid, adhesive forces make fluid molecules stick to the surface with no relative velocity between the surface and the molecule; a condition usually termed *no slip condition*. Through viscosity effects, the fluid molecules stuck to the surface, influence molecules passing by in their vicinity, essentially slowing down their pace and reducing the velocity to values below the freestream value. Further outwards from the surface, viscosity effects get replaced by turbulent shear forces, still leading to a

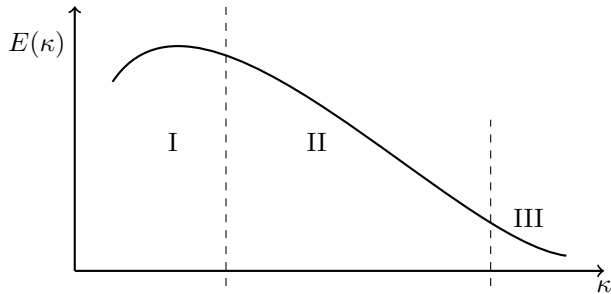


Figure 1.1: A typical energy spectrum in turbulent flows, where E is the energy per wave number and κ denotes the wave number. Large, energy-bearing eddies (I), inertial subrange (II), dissipative range (III).

retardation of the flow. This process continues until the outer edge of the boundary layer is reached (at distance δ from the solid boundary, marking the boundary-layer thickness), at which the effect of the solid boundary is no longer noticeable and the velocity remains unaltered from its freestream value. The phenomena described above lead to a velocity profile like the one shown in Fig. 1.2 including a non-zero vertical velocity gradient, which mechanically produces turbulence due to shear. One could say that turbulence is mainly generated in the boundary layers, but is not restricted to them as exemplified by wakes behind bluff bodies or other separated regions with large spatial differences in the velocity field. Since boundary layers are such an omnipresent phenomenon in engineering type of flows, a short discussion of their structure seems necessary at this point.

In general, boundary layers emerge from the leading edge of an object immersed into (uniform) fluid flow, such as a flat plate in a wind tunnel or an airfoil moving at the aircraft's speed, and are developing in both thickness and character (i.e. from laminar to turbulent) with distance downstream of the leading edge. However, here we will consider a fully-developed turbulent boundary layer, which would appear at some distance downstream of the object's leading edge. Figure 1.2 also includes the structure of a typical boundary layer over a smooth wall. There are different sublayers within the boundary layer, ranging from the viscous sublayer near the surface over the logarithmic layer to the outer turbulent layer at the upper end of the boundary layer. The buffer layer can be seen as a transition region between the viscous sublayer and the logarithmic layer. In the viscous sublayer, viscous shear dominates and the velocity profile can be approximated as linear. In the logarithmic layer, turbulent shear stresses are dominating (see Davidson [9]) and the log-law can be used to describe the velocity profile.

$$u^+ = \frac{\bar{u}}{u_*} = \frac{1}{\kappa} \ln \left(\frac{zu_*}{\nu} \right) + B, \quad (1.2)$$

where $\kappa = 0.41$ is the von Kármán constant, u_* is the friction velocity, z is the vertical coordinate, $\nu = \mu/\rho$ is the kinematic viscosity and B is a constant, often taken as 5 for flat plate boundary layers [8]. u^+ denotes the normalized velocity in wall-unit scaling. Often,

Eq. (1.2) is assumed to hold even throughout the outer turbulent layer if an additional wake function is used (see Davidson [9]).

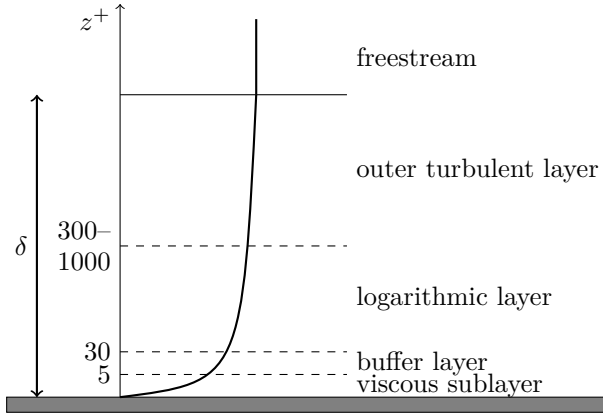


Figure 1.2: *Velocity profile in a fully-developed turbulent boundary layer above a smooth surface (not to scale). The vertical coordinate is given in wall-unit scaling as $z^+ = \frac{zu_*}{\nu}$ and δ denotes the boundary-layer thickness.*

1.2.1 The atmospheric boundary layer

One boundary layer is of particular importance for us humans, since we spend most of our lives immersed inside it; the atmospheric boundary layer. The ABL constitutes the lowest part of the troposphere and forms against the rough surface of the Earth. Even though the vertical structure of the ABL is principally similar to the one of the smooth-wall boundary layer shown in Fig. 1.2, some terminology is different and therefore the structure of the ABL is illustrated in Fig. 1.3. The thickness of the ABL varies considerably between $H \approx 100$ m during stable conditions at night and $H \approx 2000 - 3000$ m under unstable conditions caused by solar radiation during daytime [10]. A typical estimate of the thickness of the atmospheric boundary layer in neutral conditions is $H \approx 1000$ m. The lowest 10% of the ABL are usually called the surface layer [10–12] with constant¹ momentum and heat flux. In the surface layer, the influence of the Earth’s rotation on the flow is negligible and the flow is dominated by the friction forces caused by the rough ground. Analogically to the logarithmic layer in the smooth-wall boundary layer, the wind speed profile can be described in the surface layer with the help of a logarithmic law,

$$\frac{\bar{u}}{u_*} = \frac{1}{\kappa} \ln \left(\frac{z - d}{z_0} \right), \quad (1.3)$$

where z_0 is the aerodynamic roughness length of the ground and d is the zero-plane displacement. Closest to the wall resides the roughness sublayer, in which the flow is

¹ Usually it is assumed that the momentum and heat flux vary less than 10% from their surface value throughout the surface layer.

directly influenced by the geometry of the roughness elements and the wind speed profile deviates from the logarithmic form [13]. The zero-plane displacement is used in Eq. 1.3 for very rough surfaces in order to shift the ground upwards allowing to compensate for the presence of the roughness sublayer and guaranteeing that the logarithmic wind speed behavior is retained throughout the surface layer (and part of the roughness sublayer). The actual range of the roughness sublayer is not clearly defined, but 2–5 times the height of the roughness elements often serves as an estimate of the roughness-sublayer height [14, 15]. However, Florens et al. [16] report smaller values of about 1.5–1.8 times the roughness-element height. Above the surface layer, the flow is balanced by the large-scale pressure gradient, the Coriolis force and friction due to turbulence. Even though it is rarely observed in nature, the wind profile theoretically assumes a spiral pattern. The layer is named after Ekman, who mathematically derived the influence of the Coriolis force on the ABL, leading to the spiral pattern or the Ekman spiral [17].

Finally, above the ABL, we find the free atmosphere, which usually does not contain turbulence or only intermittent turbulence bursts.

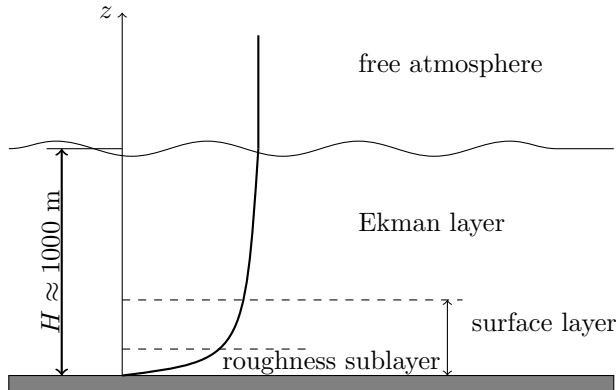


Figure 1.3: *The vertical structure of the atmospheric boundary layer (not to scale). H denotes the thickness of the atmospheric boundary layer.*

1.3 Simulation of turbulent flows

Owing to the immense importance of turbulent flows in every-day engineering problems, much research effort has been put into their investigation. Analysis of turbulent flows is in most cases not possible in an analytical way. Therefore, experiments in wind tunnels or the field are often employed for studying turbulent flows and turbulence phenomena. However, measurements need to be carefully planned and performed and even then they can suffer from difficulties that may impair the quality of the results; e.g. insertion of measurement equipment can disturb the flow, operational Reynolds numbers may not be attainable for scale models in wind tunnels, the wind-tunnel walls can influence the flow field and parts of the flow may be inaccessible for measurements. As computers are becoming progressively more powerful, the field of computational fluid dynamics

(CFD), in which turbulent flows are studied on virtual models with the help of numerical simulations, enjoys increased attention. In CFD simulations, it is easily possible to avoid the aforementioned problems that may complicate measurements. The biggest asset of CFD compared to measurements is, though, that virtual models can be generated faster and cheaper than physical prototypes, allowing design and parameter studies to be performed in a more cost- and time-efficient manner. Nevertheless, CFD cannot be used as a stand-alone design tool without experimental validation.

Turbulent flows can be simulated using a variety of different methods as detailed in Table 1.1, each of which offering unique advantages and disadvantages. Which type of turbulent flow simulation to employ depends largely on the flow problem at hand, the available computational resources and often the time pressure to hold an upcoming deadline. Generally speaking, the available methods are usually offering a trade-off between computational efficiency and numerical accuracy.

To date, steady Reynolds-Averaged Navier Stokes (RANS) simulation are still most widely used in industrial CFD applications. As indicated in Table 1.1, RANS offers the benefit of low computational cost, allowing to perform many simulations in a short time, and thus to study many different designs and to carry out parameter studies or numerical shape optimization [18]. One of the main reasons for RANS being computationally efficient is that simulations can be carried out in two-dimensional domains, despite the fact that real turbulence is always three dimensional as mentioned earlier. In contrast, all of the more advanced simulation techniques require three-dimensional domains, making these simulations considerably more costly (see Table 1.1). RANS also offers the advantage that numerous well-adjusted and validated turbulence models exist for a large variety of different flow problems. At the same time, no RANS model has emerged that is able to provide reliable results in any type of flow situation. Piomelli and Balaras [19] reason that this is due to problems in modeling the large, geometry-dependent eddies, making it impossible to develop universal models. Moreover, RANS provides merely a solution for the mean flow field and turbulence is treated in a stochastic sense only, i.e. the entire energy spectrum is modeled in terms of mean flow quantities, as indicated in Fig. 1.4. While this is acceptable in many cases, such as, for example, drag and lift prediction for vehicles or the prediction of annual mean wind speeds at a certain location for wind power production, a wide range of applications cannot be served by RANS results. Applications of such kind may be, for example, active flow control [20], the field of aeroacoustics [21] and fluid-structure interaction, in which analysis usually is based on flow fields with resolved turbulence content (such as velocity components and/or pressure), fluctuating both in space and time; a requirement that cannot be fulfilled by steady RANS simulations. Unsteady RANS (U-RANS) is able to provide time-dependent solutions including some resolved turbulence content, and could as such be deemed suitable. However, the resolved turbulence content is limited to very large eddies and thus to very low frequencies (see Fig. 1.4), which in most cases would not ensure sufficient accuracy. Consequently, one of the more advanced simulation techniques presented in Table 1.1 should be preferred.

As shown in Fig. 1.4, Direct Numerical Simulation (DNS) resolves all turbulent length and time scales, which in theory yields the most accurate result. Unfortunately, DNS is not feasible for high-Reynolds number flows, due to excessive computational demands. Piomelli and Balaras [19] estimate the number of grid points necessary for DNS to

Table 1.1: Overview of simulation methods for turbulent flows.

		turbulence resolving	3D required	readiness for industry
RANS	↑ increased efficiency ↓ increased accuracy	no*	no	yes
HRLM		yes	yes	limited
LES		yes	yes	limited
DNS		yes	yes	no

* only U-RANS

scale with $Re^{9/4}$, where Re is based on an integral scale of the flow. Accounting for a reduced time step, Davidson [9] advocates that the cost of DNS should even scale with $Re^{11/4}$. Since almost all flows of industrial importance are high- Re flows, DNS cannot be considered and its usage is usually limited to fundamental test cases at low Reynolds number, such as pipe flows [22, 23] or turbulent channel flows [24, 25]. A review on the topic of DNS is provided by Moin and Mahesh [26].

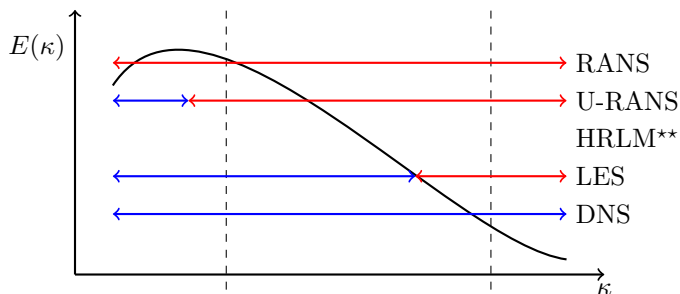


Figure 1.4: *Different simulation techniques for turbulent flow and the ranges of resolved (—) and modeled (—) turbulence.*

** Hybrid RANS/LES methods are to be found between U-RANS and LES. Their resolved turbulence content is ambiguous, since it is comparable to both U-RANS and LES in the respective regions of the computational domain.

As mentioned above, RANS methods model all turbulent scales. This task is of particular difficulty for the largest scales in the spectrum, since these usually are geometry dependent. The largest scales carry most of the energy and their accurate representation is vital for a trustworthy result. In LES, the large turbulent scales are resolved, while only the smallest scales, i.e. the ones smaller than the grid spacing, are modeled with a so-called subgrid scale (SGS) model. The grid in LES simulations should therefore be fine enough to allow for cut-off wave numbers in the inertial subrange (i.e. region II in

Fig. 1.1). Often simple SGS models are found to be sufficient as the small-scale turbulence is assumed to be of isotropic nature and thus easy to model.

The size of the large eddies is restricted by the presence of solid boundaries (i.e. an eddy cannot become larger than the distance to the nearest solid wall). Hence, when approaching a wall and inside the boundary layer, even the large eddies become comparatively small, and in order to accurately represent the turbulence in the inner part of a boundary layer, the grid needs to be prohibitively fine in all three coordinate directions. Note that the wall-normal direction has the same grid requirement in both RANS and LES, i.e. $z^+ \approx 1$ in the first grid cell, with $z^+ = zu_*/\nu$. However, the wall-parallel plane needs to be excessively fine in well-resolved LES in order to capture the streamwise stretched boundary layer structures [27]. Commonly, a grid resolution of $\Delta x^+ \approx 100$ and $\Delta y^+ \approx 20$ in the streamwise and lateral direction, respectively, is deemed necessary for LES with a well-resolved near-wall region [19]. Due to these requirements, Spalart [28] suggests to consider LES with a well-resolved near-wall region as quasi-DNS. Except for jets and flames, most industrial flows involve solid walls, which rules out well-resolved LES as a candidate for complex problems. Even though computational power is increasing dramatically nowadays, well-resolved LES is predicted to be out of reach for high- Re wall-bound flows for the next decades [28, 29]. In fact, Spalart et al. [29] estimate LES of a full aircraft wing to be infeasible until the year 2045.

As a consequence of that, strategies have been developed to make turbulence-resolving simulations available for complex flow problems at high Reynolds numbers. Methods evolved that avoid the main bottleneck, namely resolving the near-wall region. Two fundamentally different approaches are considered in this work: LES with a wall function and hybrid RANS/LES methods. Both approaches are described in more detail in Section 2.3.

2 Turbulence-resolving simulation techniques

In this chapter, the equations governing turbulent flow are introduced. Moreover, turbulence-resolving simulation techniques feasible for engineering applications are explained. Finally, a brief description of the models employed in this work is given.

2.1 Governing equations

It is widely accepted that the Navier-Stokes equations accurately describe the behavior of fluid flows, although no mathematical prove exists for their universal validity yet. For an incompressible fluid with constant density and viscosity, the instantaneous Navier-Stokes equations can be written as

$$\frac{\partial u_i}{\partial x_i} = 0, \quad (2.1a)$$

$$\frac{\partial u_i}{\partial t} + u_j \frac{\partial u_i}{\partial x_j} = -\frac{1}{\rho} \frac{\partial p}{\partial x_i} + \frac{\partial}{\partial x_j} \left(\nu \frac{\partial u_i}{\partial x_j} \right), \quad (2.1b)$$

where p denotes the hydrodynamic pressure and u_i denotes the velocity component in the i th coordinate direction ($i = 1, 2, 3$). Note that a right-handed coordinate system is assumed with $x_3 = z$ pointing vertically upwards.² Equation (2.1a) is the continuity equation and describes the conservation of mass, while Eqs. (2.1b) are the momentum equations describing the conservation of momentum. Note that the incompressible form of the Navier-Stokes equations is given here, while in Papers A and B, the compressible form was solved.

It is possible to solve the Navier-Stokes equations numerically using DNS and resolving the entire energy spectrum in Fig. 1.1. DNS requires to resolve even the smallest eddies and is therefore, as mentioned previously, limited to low Reynolds number flows and is in general not feasible for applications of industrial importance.

Different simplifications exist to enable solving Eqs. (2.1) in an affordable manner, one of which is the Reynolds decomposition that splits up an instantaneous quantity, ϕ , into a time-averaged mean value, $\bar{\phi}$, and a superimposed fluctuation, ϕ' , as in

$$\phi = \bar{\phi} + \phi'. \quad (2.2)$$

Inserting Eq. (2.2) into the Navier-Stokes equations, results, after some manipulation (see [9] for details), in the incompressible RANS equations, viz.

$$\frac{\partial \bar{u}_i}{\partial x_i} = 0, \quad (2.3a)$$

$$\frac{\partial (\bar{u}_i \bar{u}_j)}{\partial x_j} = -\frac{1}{\rho} \frac{\partial \bar{p}}{\partial x_i} + \frac{\partial}{\partial x_j} \left(\nu \frac{\partial \bar{u}_i}{\partial x_j} + \frac{1}{\rho} \tau_{ij} \right). \quad (2.3b)$$

² This definition is used throughout the thesis and in Papers D–F. In Papers A–C, the vertical coordinate direction is denoted by $x_2 = y$.

Solving these equations yields a solution for the time-averaged mean flow field instead of the instantaneous flow field described by the Navier-Stokes equations. It can be seen that an additional term appears on the right-hand side of Eq.(2.3b), compared to Eq. (2.1b). This term is called the Reynolds stress tensor,

$$\tau_{ij} = -\rho \left(\overline{u'_i u'_j} \right). \quad (2.4)$$

The Reynolds stresses constitute six additional unknowns, making the system of equations given by Eqs. (2.3a) and (2.3b) impossible to solve; a dilemma referred to as the closure problem. In order to close the system of equations, the Reynolds stresses need to be modeled. For that purpose, Boussinesq’s hypothesis [30] is often invoked, assuming that turbulent diffusion can be modeled with the help of a turbulent or eddy viscosity in analogy to molecular diffusion, which is governed by the molecular viscosity. Turbulence models based on the Boussinesq hypothesis are also referred to as eddy-viscosity models.

2.2 The LES framework

The central assumption in LES is that it is possible to divide turbulent motions of a flow into large- and small-scale motions. It is further assumed that the large-scale motions are the ones that carry most of the turbulent kinetic energy and anisotropy, while the small scales are more universal in nature and are mainly responsible for energy dissipation. In LES, the large scales are explicitly resolved and the small scales are modeled. Capturing only the large scales and modeling the small scales should in principle allow for a more accurate simulation (as compared to RANS). As such, LES is in particular suitable for the simulation of flows including spatially large turbulent motions, such as the separated flows around and behind bluff bodies.

The distinction between large and small scales is usually achieved in terms of a filtering operation. Different filtering operations exist; the most common ones being the box filter, the Gaussian filter and the spectral cut-off filter [31]. Spectral cut-off filters are most naturally used in spectral LES methods, while in finite-volume based LES, box filters are almost always used. In finite-volume methods, the filtering is implicitly done through the spatial discretization scheme. However, in meteorology, where pseudospectral methods are often employed, also explicit filtering is common. Explicit filtering has to happen at filter sizes larger than the grid size. Often, the smallest scales are referred to as the subgrid scales (SGS), even though subfilter scales (SFS) may be a more appropriate description, as advocated by Pope [31], since the filtering does not necessarily happen at grid scale. However, implicit grid filters are exclusively employed in this work and therefore the acronym SGS will be used.

In order to perform LES, the filter width should be such that at least all anisotropic, energy-bearing scales are resolved. Consequently, the cut-off wave number of the filter should be placed within the inertial subrange of the turbulence spectrum (region II of Fig. 1.1). When the cut-off resides in the inertial subrange, fairly simple SGS models are sufficient for the description of the unresolved scales, since these are more isotropic and homogeneous in nature.

Similar to the Reynolds decomposition, the instantaneous flow field can be expressed as

$$\phi = \bar{\phi} + \phi'', \quad (2.5)$$

where the instantaneous variable ϕ is decomposed into a resolvable part, $\bar{\phi}$, and an unresolved SGS fluctuation, ϕ'' . Note, that we switch notation and that the overbar now denotes a filtered or resolved quantity, while angular brackets are used from now on to denote time averaging. Introducing this definition into Eqs. (2.1a) and (2.1b) yields the filtered, incompressible Navier-Stokes equations,

$$\frac{\partial \bar{u}_i}{\partial x_i} = 0, \quad (2.6a)$$

$$\frac{\partial \bar{u}_i}{\partial t} + \frac{\partial (\bar{u}_i \bar{u}_j)}{\partial x_j} = -\frac{1}{\rho} \frac{\partial \bar{p}}{\partial x_i} + \frac{\partial}{\partial x_j} \left(\nu \frac{\partial \bar{u}_i}{\partial x_j} + \frac{1}{\rho} \tau_{ij} \right), \quad (2.6b)$$

which appear to be identical to Eqs. (2.3a) and (2.3b), except for the time derivative on the left-hand side of Eq. (2.6b) and the different meaning of the overbars (time averaging vs. filtering). The additional stress term on the right-hand side is now referred to as the SGS stress tensor and reads

$$\tau_{ij} = -\rho (\overline{u_i u_j} - \bar{u}_i \bar{u}_j). \quad (2.7)$$

If eddy-viscosity based models are used, the stress tensors in Eqs. (2.4) and (2.7) can be modeled as

$$\tau_{ij} - \frac{1}{3} \tau_{kk} \delta_{ij} = -\nu_t \left(\frac{\partial \bar{u}_i}{\partial x_j} + \frac{\partial \bar{u}_j}{\partial x_i} \right) = -2\nu_t \bar{S}_{ij}, \quad (2.8)$$

where ν_t is the eddy or turbulent viscosity and $\bar{S}_{ij} = \frac{1}{2} \left(\frac{\partial \bar{u}_i}{\partial x_j} + \frac{\partial \bar{u}_j}{\partial x_i} \right)$ is the strain rate tensor. Note that the stress tensors in RANS and LES are modeled in the same way in the framework of an eddy-viscosity model. Therefore, from a numerical point-of-view, the difference between RANS and LES can be traced back to different definitions of the eddy viscosity. In principle, one could say that (U-)RANS and LES differ in the magnitude of the eddy viscosity, with LES exhibiting much lower values of ν_t than (U-)RANS. This realization will be of practical importance later in Sections 2.4.2 and 2.4.3 for the description of hybrid RANS/LES methods.

Chapman [32] as well as Piomelli and Balaras [19] estimate the grid point requirement for a well-resolved LES of a flat-plate boundary layer to scale with $Re^{9/5}$, while Choi and Moin [33] propose $Re^{13/7}$ to be more accurate. In any case, this indicates that well-resolved LES is only attainable for moderately high Reynolds numbers. As mentioned before, most flow problems of engineering relevance involve high or very high Reynolds numbers, making LES with a well-resolved near-wall region infeasible. Hence, in order to enable LES for high- Re flows, special treatment of the main bottleneck, i.e. the region near solid walls, is required. Two possible approaches are described in Section 2.3.

In order to numerically solve Eqs. (2.6), the equations need to be discretized. Most often finite-volume methods with second-order accurate spatial and temporal discretization are employed in general purpose CFD. For details regarding the discretization process, see e.g. Ferziger and Peric [34]. Here, finite-volume methods are exclusively used, but it

should be mentioned that different approaches to CFD exist, including, for example, finite differences, finite elements, as well as spectral and pseudospectral methods. In particular, the latter offer the advantage of high numerical accuracy and efficiency for a given grid. Fornberg [35] derives the pseudospectral method as the limiting case of a finite-difference discretization with infinite accuracy.³ Unfortunately, pseudospectral methods require an equidistant grid spacing and are limited to flow problems that can be treated with periodic boundary conditions. These restrictions make pseudospectral methods infeasible for general purpose CFD and explain the popularity of the more versatile finite-volume based methods. Pseudospectral methods are often employed for approximating gradients in the horizontal directions in LES of the ABL (e.g. [36–39]). Due to the non-periodic boundaries at the ground and at the upper end of the domain and possible vertical grid stretching, vertical gradients are, however, still discretized using second-order accurate central differencing schemes.

An alternative to pseudospectral methods can be the use of higher-order discretization schemes in the finite-volume method, also offering higher numerical accuracy and efficiency on a given grid. Higher-order numerics have proven useful in hybrid RANS/LES simulations by Kok and van der Ven [40] for the flow over a rounded bump in a square duct and a delta wing. Higher-order schemes have also been used in DNS and LES by Morinishi et al. [41] and by Davidson and Andersson [42], and showed to yield improved results compared with standard second-order discretization schemes. In both pseudospectral and higher-order finite-volume methods, the gain in numeric efficiency is due to the fact that superior results can be obtained on a given grid. In other words, equally good results can be obtained on a coarser grid with pseudospectral methods or higher-order discretization schemes compared to a standard second-order accurate finite volume discretization.

2.3 Treatment of the near-wall region

In this section, two fundamentally different approaches for avoiding to resolve the near-wall region in LES of high- Re wall-bounded flows are presented.

2.3.1 LES with a wall function

One way to avoid resolving the near-wall region in LES is to specify the wall-shear stress, $\tau_w = \rho u_*^2$, based on the log-law, similarly to the use of wall functions in RANS modeling. In that case, the friction velocity needs to be determined, which can be done iteratively from Eq. (1.2) for smooth-wall boundary layers or explicitly from Eq. (1.3) for the case of rough-wall boundary layers. For the simulation of the ABL, for example, the wall-shear stress is based on the local horizontal wind speed, $U_{par} = \sqrt{\bar{u}^2 + \bar{v}^2}$, at the first vertical grid point, $\Delta_z/2$, and the total wall-shear stress can be split into its horizontal components as

$$\tau_{i3,w} = -\rho \left[\frac{U_{par}\kappa}{\ln[(\Delta_z/2)/z_0]} \right]^2 \frac{\bar{u}_i(x, y, \Delta_z/2)}{U_{par}}, \quad (i = 1, 2). \quad (2.9)$$

³ Note that, on equidistant, Cartesian grids, the finite-difference and finite-volume methods are identical.

Such a formulation can be applied only in relatively simple cases, for which the wall-shear stress can be determined from the mean flow. A requirement for the above formulation to hold is that the first grid cell needs to be larger than the zero-plane displacement. In the roughness sublayer and below the height d , the velocity profile deviates from the logarithmic form and therefore Eq. (2.9) would be inappropriate. Figure 2.1 illustrates the difference in grid resolution near the wall in well-resolved LES and LES with a wall function. In the latter case, Eq. (2.9) is used to prescribe the wall-shear stress.

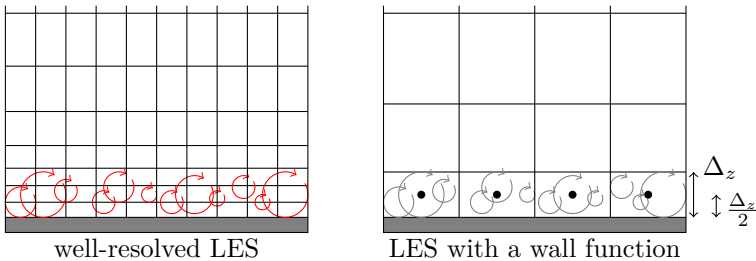


Figure 2.1: *Wall-region in well-resolved LES and LES with a wall function. Resolved eddies and unresolved eddies are shown in red and gray, respectively. The centers of the first off-wall cell are also indicated for the LES with a wall function.*

2.3.2 Hybrid RANS/LES methods

Another way of avoiding to resolve the near-wall region in LES is to employ hybrid RANS/LES methods. Actually, the expression hybrid RANS/LES method is somewhat misleading, since these methods couple LES and U-RANS rather than LES and steady RANS. However, in agreement with common terminology, the expression RANS will be used here.

Fairly coarse grids may be sufficient for resolving the large, energy-bearing eddies and hence for capturing the relevant physics of flows dominated by large-scale turbulence, such as bluff-body flows and wake flows in general. At the same time, RANS models have been successfully used for the simulation of attached boundary layers for decades and are consequently well-adjusted and validated for these types of flows. One central idea of hybrid RANS/LES approaches is therefore to use RANS in the attached boundary layers and to employ LES away from solid boundaries and in separated flow regions. In this way, it is possible to combine the best features of both RANS and LES and to enable turbulence-resolving simulations for engineering-type of flows involving complex geometries and high Reynolds numbers. Due to the usage of RANS in the boundary layer, the grid in the wall-parallel plane can be relaxed from the stringent requirements for well-resolved LES. Note that the treatment of the near-wall region in hybrid RANS/LES simulations is fundamentally different from the simple model presented in Section 2.3.1. While the wall function is applied only in the first grid cell at the wall, hybrid RANS/LES methods aim to treat the entire boundary layer in RANS mode.

Following the above idea, Spalart et al. [29] introduced the first hybrid RANS/LES method in 1997, termed Detached-Eddy Simulation (DES). DES uses a so-called global

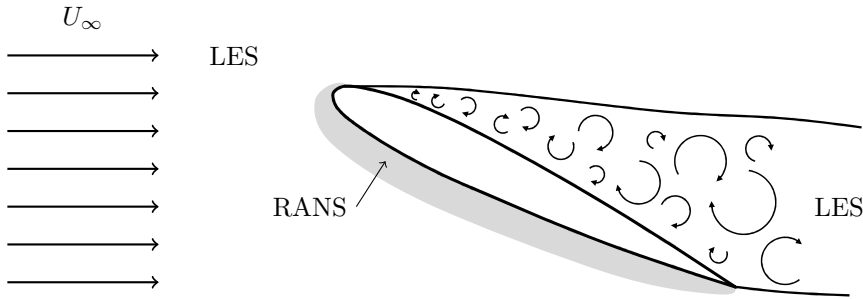


Figure 2.2: *Schematic drawing of a hybrid RANS/LES method for an airfoil in deep stall. The attached boundary layer on the pressure side of the airfoil is treated in RANS mode, as indicated by the shaded area. The remainder of the flow, in particular the separated flow on the suction side of the airfoil, is treated in LES mode.*

approach in which the model itself decides whether the LES or RANS mode should be activated in a certain region of the grid. This decision is made based on a comparison of the local grid spacing and the wall distance. In order to ensure the desired behavior (i.e. RANS in boundary layers and LES otherwise), DES grids have to be carefully designed. That is, the grid spacing in the wall-parallel plane has to exceed the local boundary layer thickness, δ . Originally, DES was invented for the use in massively separated flows, such as an airfoil in deep stall⁴. In such a case, the attached boundary layers are thin and the separated region is dominated by large-scale turbulence. A schematic drawing of such a case is provided in Fig. 2.2.

It has been anticipated by Spalart et al. [29] that in case of thick boundary layers or uncaredful grid generation, the wall-parallel grid spacing can become smaller than the boundary-layer thickness and a phenomenon called Modeled Stress Depletion (MSD) can occur. If the LES mode is activated inside the boundary layer, the length scale is reduced, which in turns leads to a decrease in eddy viscosity. Consequently, the modeled stresses are reduced, even though the grid is not fine enough to support resolved stresses. Due to the subsequent reduction of skin friction caused by MSD, premature separation can occur in severe cases, as shown by Menter and Kuntz [43, 44]. This phenomenon of premature separation is termed Grid Induced Separation (GIS). Initial solutions to MSD and GIS have been proposed by Menter and Kuntz [43], who suggest using a shielding function for the boundary layer, and by Deck [45], who proposes to make the DES approach zonal, i.e. disable the DES limiter in critical regions. In 2006, a nowadays commonly used remedy, termed Delayed DES (DDES), was presented by Spalart et al. [46]. Based on the idea of Menter and Kuntz [43], the RANS mode is preserved in the boundary layer with a shielding function.

As an effort to reduce the influence of the RANS model in global hybrid RANS/LES methods, wall-modeled LES (WMLES) has been proposed. In comparison to DES or

⁴ Stall is the sudden loss of lift force as a consequence of flow separation. Flow separation increases the pressure on the upper side of the wing and therefore the lift force is drastically reduced.

DDES, the switch from RANS to LES is performed much closer to the wall in WMLES, i.e. inside the boundary layer. This can only be done, if the grid allows for resolved boundary-layer turbulence, so that the problem of MSD will be avoided. Consequently, a greater portion of the turbulence is resolved in WMLES and the influence of the RANS model is restricted to a narrow region near the wall. One strategy for WMLES, termed Improved DDES (IDDES), has been proposed in 2008 by Shur et al. [47]. The basic idea of IDDES is for the model to act as WMLES, if the inflow conditions and the grid support such behavior. The inflow conditions must contain turbulent content and the grid is required to be fine enough to resolve boundary-layer eddies. In case those prerequisites are not fulfilled, IDDES will perform as conventional DDES.

Hybrid RANS/LES simulations can also be carried out in a zonal fashion. That is, designated zones that are treated in RANS or LES mode are specified a-priori. These zones can principally be defined in two ways. Firstly, the near-wall region can be specified as a RANS region, which leads to a situation similar to the one shown in Fig. 2.3a. The interface between RANS and LES is then prescribed at a constant grid line parallel to the wall as exercised by Davidson and Dahlström [48] and Davidson and Peng [49]. Secondly, based on the idea that most of the flow in a large domain can be treated as (quasi-) steady RANS, it is also possible to only specify LES in a small region of interest. In that case, the LES zone is surrounded by RANS regions and these kind of approaches are also referred to as Embedded LES (see Fig. 2.3b). By careful design of RANS and LES regions, zonal methods can provide safety from MSD and GIS.

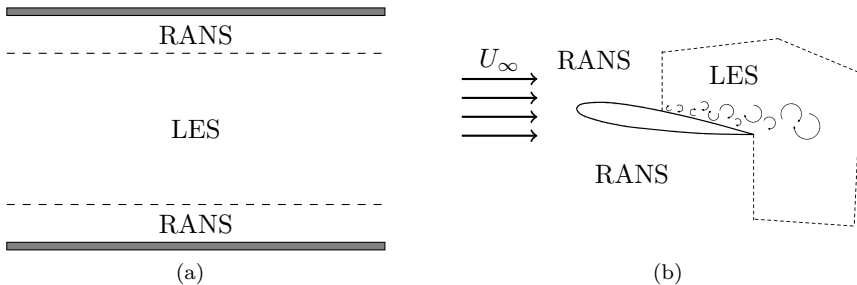


Figure 2.3: *Schematic drawing of two zonal hybrid RANS/LES methods. In a), the interface is specified along a grid line or with constant distance to the surface. In b), RANS is used everywhere, except in a specified focus region.*

One big problem in all hybrid RANS/LES methods is the existence of a certain "gray area" at the interface between RANS and LES, as described by Spalart [50]. In this gray area, the computation cannot really be considered RANS, as the eddy viscosity and, subsequently, also the modeled stresses are gradually decreased. At the same time, no (or very little) resolved stresses are present, as they either have to come from the RANS region or have to gradually build up. The gray area can hence lead to substantial delays in the formation of instabilities and three-dimensional turbulence content. Moreover, high values of eddy viscosity may be convected from upstream RANS into downstream LES regions, which amplifies the delay in the formation of LES content. Cases with a

geometrically defined separation location usually suffer less from the gray area issue than cases with shallow separation. Faster development of turbulence structures and hence a mitigation of the gray area problem has been achieved in several ways, among others, changing the LES length scale [51, 52], high-pass filtering the velocity field and basing the SGS model on the fluctuating velocity field [53], accounting for energy backscatter [54, 55] and randomizing the eddy-viscosity field [56].

In zonal approaches, an obvious solution to the gray-area issue is to introduce LES content at the RANS/LES interface, since the interface location is known. This procedure is known as forcing and is similar to providing unsteady inlet conditions for LES or DNS. The injected turbulent content can, for example, stem from either synthetic turbulence, as described by Davidson and Billson [57], or from a precursor DNS as in [48]. In some cases [58, 59] also "recycled" fluctuations from a downstream location have been successfully injected. Note that such a treatment is not applicable to global methods, as the interface location is not known a-priori and might even be time-dependent.

2.4 Models used in this thesis

Here, the k -equation SGS model used in LES with a wall function and two different hybrid RANS/LES approaches employed in this thesis are briefly described.

2.4.1 Deardorff's k -equation SGS model

In LES of the ABL, the one-equation model proposed by Deardorff [60] has gained much attention [38, 61] and modified versions have been employed for the simulation of forest canopies [62–64]. This model was used for the simulations on which Papers C–F are based.

The model involves the SGS turbulent kinetic energy (TKE) and hence its transport equation needs to be solved, reading,

$$\frac{\partial k}{\partial t} + \frac{\partial(\bar{u}_j k)}{\partial x_j} = \frac{\partial}{\partial x_j} \left[\left(\nu + \frac{\nu_t}{\sigma_k} \right) \frac{\partial k}{\partial x_j} \right] + P_k + P_b - \varepsilon, \quad (2.10)$$

where k is the subgrid scale turbulent kinetic energy, P_k , P_b and ε , are its production due to shear and buoyancy and its dissipation rate, respectively and $\sigma_k = 0.5$. The production of SGS TKE due to shear reads,

$$P_k = \nu_t \left(\frac{\partial \bar{u}_i}{\partial x_j} + \frac{\partial \bar{u}_j}{\partial x_i} \right) \frac{\partial \bar{u}_i}{\partial x_j}, \quad (2.11)$$

and the production of SGS TKE due to buoyancy reads,

$$P_b = \frac{g}{\theta_0} \tau_{3\theta}. \quad (2.12)$$

The eddy viscosity, necessary for parameterization of the SGS stress in Eq. (2.8), is computed as the product of a length scale, l , and a velocity scale, \sqrt{k} , viz.

$$\nu_t = 0.1 \sqrt{k} l \quad (2.13)$$

To allow a reduction of the length scale in stable stratification, l is defined by

$$l = \min \left(0.76\sqrt{k} \left(\frac{g}{\theta_0} \frac{\partial \bar{\theta}}{\partial z} \right)^{-1/2}, \Delta \right), \quad (2.14)$$

whenever $\partial \bar{\theta} / \partial z > 0$. In Eq. (2.14), $\bar{\theta}$ denotes potential temperature and $\Delta = (\Delta_x \Delta_y \Delta_z)^{1/3}$ is the cubic root of the grid cell volume and the classical filter width in LES. The SGS heat flux, $\tau_{i\theta}$ is defined similarly to the SGS stress tensor as,

$$\tau_{i\theta} = -\nu_h \frac{\partial \bar{\theta}}{\partial x_i}, \quad (2.15)$$

where ν_h is the eddy diffusivity for heat defined by

$$\nu_h = (1 + 2l/\Delta)\nu_t. \quad (2.16)$$

Finally, the dissipation rate, ε , is modeled as [60],

$$\varepsilon = (0.19 + 0.51l/\Delta) \frac{k^{3/2}}{l}. \quad (2.17)$$

In the production term in Eq. (2.11), the velocity gradients need to be computed. Usage of the wall function described in Eq. (2.9) makes it necessary to adapt the vertical gradients in the first grid point off the wall. From Eq. (1.3), the correct vertical gradient can be derived, assuming that $d = 0$, as,

$$\frac{\partial \bar{u}_i}{\partial z} = \frac{u_*}{\kappa z} \frac{\bar{u}_i(x, y, \Delta_z/2)}{U_{par}}, \quad (i = 1, 2). \quad (2.18)$$

2.4.2 DES based on the SA model (SADES)

In Paper A, the original version of DES [29] based on the Spalart-Allmaras (SA) one-equation RANS model [65] was employed. Note that even though the original version is described here, DES can be implemented for any underlying RANS model.

A single transport equation for a viscosity-like quantity, $\tilde{\nu}$, is solved in the SA RANS model with a destruction term proportional to

$$\varepsilon_{\tilde{\nu}} \propto \left(\frac{\tilde{\nu}}{d_w} \right)^2, \quad (2.19)$$

where d_w denotes the distance to the nearest wall. Recall that the main difference between RANS and LES, from a numerical point-of-view, can be found in the magnitude of eddy viscosity and that RANS models will yield significantly larger levels than SGS models. Therefore, any RANS model can be transformed into a SGS model by adapting the eddy viscosity. In the present model, increasing the destruction term leads to a decrease in eddy viscosity, essentially turning the model into a SGS model. In order to achieve the desired behavior, d_w is replaced with a modified length scale, \tilde{d} , based on the local grid spacing, Δ , as in

$$\tilde{d} = \min(d_w, C_{DES}\Delta), \quad (2.20)$$

where $C_{DES} = 0.65$ is the DES constant [29]. Now, the altered model will act as a RANS model, when $d_w < \Delta$ and as a SGS model, when $d_w > \Delta$. The switch between RANS and LES is thus dependent on the local grid resolution. In DES, Δ is taken as the maximum edge length of the control volume, i.e. $\Delta = \Delta_{max} = \max(\Delta_x, \Delta_y, \Delta_z)$. The RANS requirement on the grid spacing in the boundary layer leads to anisotropic grids near the wall, where $\Delta_x \approx \Delta_y \gg \Delta_z$. Subsequently, d_w is likely to be smaller than Δ here and hence RANS behavior is obtained as desired. Outside the boundary layer, the grid spacing is likely to be more isotropic and $\Delta \ll d_w$, which modifies the length scale and decreases the levels of eddy viscosity (by increasing $\varepsilon_{\bar{\nu}}$). As a consequence, SGS model behavior is obtained. Bear in mind that the basic idea of DES is to treat the entire boundary layer in RANS mode. Hence the requirement for correct behavior is that the grid spacing in the wall-parallel plane exceeds the local boundary layer thickness, δ . As mentioned earlier, ambiguous grids with a wall-parallel spacing Δ_{max} smaller than δ lead to the problems of MSD and GIS.

2.4.3 An algebraic hybrid RANS/LES model (HYB0)

In Papers A and B, a hybrid RANS/LES method developed by Peng [66, 67] was used. It is an algebraic hybrid RANS/LES model combining a mixing-length RANS model in the near-wall region with the Smagorinsky SGS model [68] in the off-wall LES region. As no additional transport equation has to be solved in this model, we also refer to it as a zero-equation hybrid RANS/LES model or the HYB0 model.

Simple algebraic RANS models have proved to be robust and efficient in modeling attached boundary layers, as, for example, by Baldwin and Lomax [69]. Due to the simplicity of the model, shorter computation times are achieved by the HYB0 model as compared to DES based on one- or two-equation RANS models.

In the near-wall RANS mode, the eddy viscosity is formulated according to the mixing-length concept as

$$\tilde{\nu}_t = \tilde{l}_\nu^2 \bar{S}, \quad (2.21)$$

where \tilde{l}_ν is the turbulent length scale being proportional to the wall distance, d_w , and is defined by

$$\tilde{l}_\nu = f_\nu \kappa d_w. \quad (2.22)$$

In the above equation, f_ν represents an empirical damping function, based on the viscosity ratio in the RANS region $R_t = \tilde{\nu}_t / \nu$. The damping function reads

$$f_\nu = \tanh\left(\frac{R_t^{1/3}}{2.5}\right). \quad (2.23)$$

Away from the wall, in the LES region, the Smagorinsky SGS model is employed with the SGS eddy viscosity as follows

$$\nu_{SGS} = (C_s \Delta_{Hyb0})^2 \bar{S}, \quad (2.24)$$

with $C_s = 0.12$ and

$$\Delta_{Hyb0} = \sqrt{\frac{(\Delta_{max}^2 + \Delta^2)}{2}}. \quad (2.25)$$

A crucial step in developing efficient hybrid RANS/LES models is the design of the interface between the two modes. Here, the RANS length scale, \tilde{l}_ν , is modified over the RANS/LES interface by multiplying with an empirical matching function, i.e. $l_\nu = \tilde{l}_\nu f_s$. This results in the following eddy viscosity in the RANS region

$$\nu_t = l_\nu^2 \bar{S}. \quad (2.26)$$

The matching function, f_s , reads

$$f_s = \frac{1}{2} \left[\exp\left(-\frac{R_s^{0.75}}{4.75}\right) + \exp\left(-\frac{R_s^{0.3}}{2.5}\right) \right], \quad (2.27)$$

with $R_s = \tilde{\nu}_t/\nu_{SGS}$ being the ratio of the eddy viscosities in the RANS and LES regions. Finally, the hybrid eddy viscosity, ν_h , is chosen according to

$$\nu_h = \begin{cases} \nu_t, & \text{if } \tilde{l}_\nu < \Delta_{Hyb0}, \\ \nu_{SGS}, & \text{if } \tilde{l}_\nu \geq \Delta_{Hyb0}. \end{cases} \quad (2.28)$$

3 Applications

As mentioned earlier, steady RANS simulations are still widely used in industry for predicting turbulent flows. However, there are many engineering problems involving transient flow phenomena, in which RANS naturally cannot be employed. Typical examples are often found in the fields of noise prediction, active flow control and fluid-structure interaction and are therefore relevant for almost all industrial applications. In these cases, turbulence-resolving methods have to be invoked. These are by default unsteady methods and are thus able to provide time-dependent flow information. Using turbulence-resolving simulation techniques allows for in-depth studies of transient flow phenomena and opens up the possibility for multidisciplinary analysis. Prediction of the flow itself may not always be the prime objective and the time-dependent flow information may be used as input for subsequent analysis. Two examples of such multidisciplinary applications are the field of computational aeroacoustics and fluid-structure interaction simulations. In the former, the simulation of the flow field provides the noise source (turbulent velocity and pressure fluctuations), while in the latter, the flow field and the resolved turbulence serve as input for analysis of the structural loads.

Two multidisciplinary applications of engineering importance were studied in this thesis and will be presented in Sections 3.1 and 3.2. Firstly, the aerodynamic noise radiation from a multi-element airfoil was investigated with the help of hybrid RANS/LES simulations and, secondly, the wind-induced fatigue loads of wind turbines in forest regions were studied based on LES with a wall function.

3.1 Aerodynamic and aeroacoustic analysis of a multi-element airfoil

Many people are familiar with the sudden increase in noise inside an airplane, towards the end of a flight, when the approach phase is initiated. This increased noise level can be pin-pointed to the deployment of high-lift devices on the airplane's wings, often including a leading-edge slat and a trailing-edge flap. The latter are used both to increase the wing's lift force at the reduced airspeed during the approach phase and to prevent stall by reducing the effective angle of attack (AoA). Since the engines are in idle during the approach phase, and due to the proximity to the ground, noise from the high-lift system must not be neglected and offers possibilities for optimization. In the last decades, air traffic has constantly been increasing and is projected to further grow in the near future. At the same time, population densities in central Europe are relatively high and airports are often located in close proximity to residential areas. In order to protect the residents from the aircraft noise, regulations have been set-up by the International Civil Aviation Organization (ICAO). As of today, the radiated noise levels of all aircraft need to fulfill the requirements stated in Annex 16 of the Convention of International Civil Aviation [70], in order to be certified by the ICAO. Since the regulations are becoming more and more stringent, the aircraft noise prediction and reduction have earned increased interest of the aircraft industry and airlines. For that reason, better understanding of the noise

generation through the high-lift system may enable optimized designs and more silent aircraft.

Moreover, the flow around multi-element airfoils with deployed high-lift devices is inherently turbulent and complex, as a number of flow phenomena are present simultaneously and also interact with each other. The flow phenomena include shallow boundary layers, multiple wakes, flow impingement, re-circulation zones, stagnation points and flow separation, making the simulation of multi-element airfoils a challenging test case from a turbulence-modeling point-of-view.

Hybrid RANS/LES techniques were employed for the simulation of the flow field around the three-element airfoil shown in Fig. 3.1. The airfoil is the F15 model, developed by DLR (German Aerospace Center). From a cut through the high-lift wing of a generic short- to medium-range aircraft with twin engines, a two-dimensional model of the three-element airfoil is obtained [71]. As compared to the clean wing, the slat and flap are deflected downwards by 28.8° and 38.3° , respectively, which is representative of a landing configuration. From a manufacturing point-of-view, all of the three airfoil elements exhibit blunt trailing edges. This is accounted for in the computations at all trailing edges, except for the slat cusp, which is artificially sharpened.

Based on the results of the flow simulation, an aeroacoustic analysis was also performed. The objectives of the study were manifold: to gain more insight into the complex flow field and to assess the feasibility of hybrid RANS/LES techniques for high- Re simulations as well as to investigate the possibility of decoupling the flow and aeroacoustic simulations and to evaluate the farfield noise signature of the entire airfoil.

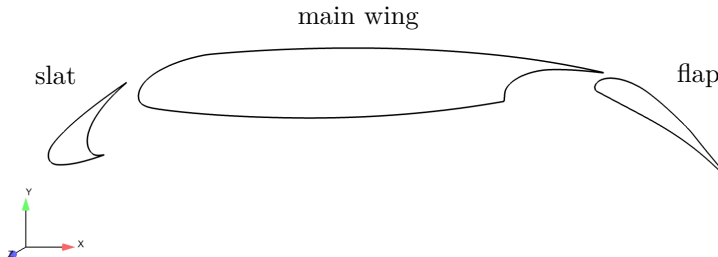


Figure 3.1: *Geometrical definition of the DLR F15 three-element airfoil with leading-edge slat and trailing-edge flap.*

The situation of airframe noise being radiated from the aircraft towards observers at the ground is sketched in Fig. 3.2. Ideally, the noise levels at the observer locations would be predicted solely by the hybrid RANS/LES simulation without involving additional tools for predicting the noise radiation. Due to the separation of scales involved, this is unfortunately not possible. Noise or sound is transported through pressure waves and in order to propagate the noise from the airfoil to the observers, a computational grid fine enough to resolve the pressure waves is necessary. A conservative estimate is that 20 cells are required to resolve one wavelength [72]. Considering the high-frequency noise typically reaching frequencies up to 5000–8000 Hz, the smallest wavelength to be resolved is approximately 5 cm, which translates into a constant grid spacing of about 3.5 mm.

Since the observers are situated several hundreds of meters away from the airfoil, enormous computational efforts would be required. Additionally, higher-order discretization schemes with low numerical diffusion and dispersion may be needed to not dissipate the pressure waves or contaminate them with numerical noise.

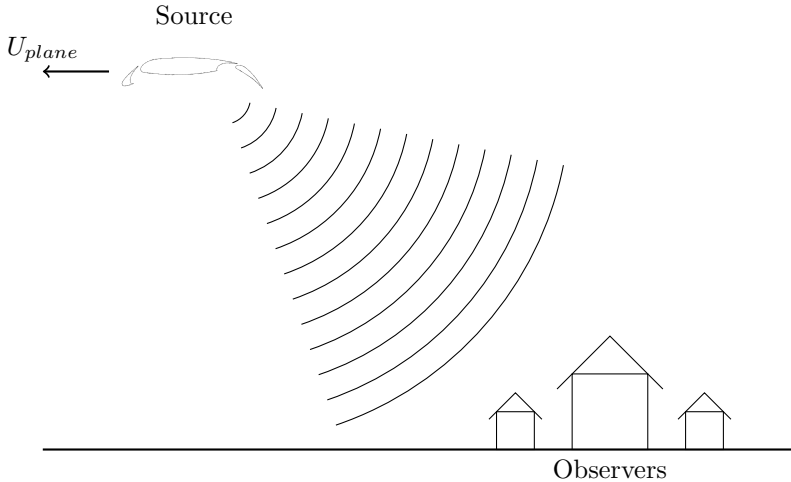


Figure 3.2: *Sketch of airframe noise radiation.*

As a remedy, the simulations of the flow and the noise propagation are decoupled, meaning that the hybrid RANS/LES simulation and the aeroacoustic simulation are performed in two separate steps. Therefore, the computational grid can be restricted to the nearfield of the airfoil, and a sufficient grid resolution for capturing the important flow effects can be guaranteed. In order to compute the noise propagation from the airfoil to the farfield observers, so-called acoustic analogies are employed.

In the following, a short review of previous hybrid RANS/LES simulations for high-lift airfoils and the aeroacoustic assessment is given. Thereafter follows a description of the work flow for decoupled aerodynamic and aeroacoustic analysis for multi-element airfoils as well as a presentation of typical results.

3.1.1 Previous work

In 2002, Rumsey and Ying [73] published a comprehensive review of the CFD capabilities in predicting high-lift flow fields. By that time, almost all research activities were focused on steady RANS simulations. Rumsey and Ying identified the inclusion of unsteady effects in high-lift flows as an important next step towards more reliable CFD predictions. Khorrami et al. [74] were one of the first to perform transient simulations on a high-lift wing. They made a two-dimensional U-RANS simulation of a three-element airfoil and focused on the flow, as well as on the nearfield acoustics of the slat-cove region. Singer et al. [75] then performed an acoustic analysis of the farfield noise using the Ffowcs-Williams and Hawkings (FWH) method based on the simulation results of Khorrami et al. In a

follow-up study, Khorrami et al. [76] report that the U-RANS method is too diffusive to allow the shear-layer instabilities to survive and to grow, which prompted them to incorporate forcing in the boundary layer upstream of the slat cusp. In the same study, also the farfield noise was studied using the FWH analogy.

Following the rapid increase in computational power and the development of hybrid RANS/LES methods, many groups have performed turbulence-resolving simulations on quasi-two-dimensional multi-element airfoils with deployed high-lift devices. Terracol et al. [77, 78] used a zonal hybrid RANS/LES approach, where first a two-dimensional RANS simulation is carried out for the entire geometry. In a second step, turbulence-resolving simulations are then run in a limited focus region. Here, the turbulence-resolving simulation was restricted to the slat-cove region. Deck [79] also used a zonal hybrid RANS/LES method, but computed the entire three-dimensional unsteady flow field around the three-element airfoil. Choudhari and Khorrami [80] and Lockard and Choudhari [81] employed U-RANS, but switched off the turbulence model in the slat cove. Thus, they are essentially using a zonal method of RANS and implicit LES⁵. Also in [82–86], zonal hybrid approaches are used. However, global methods were used by Knacke and Thiele [87] and Reuß et al. [88]. Pure LES was tested by Ma and Zhang [89] and König et al. [90].

In terms of aeroacoustic analysis based on the turbulence-resolving simulations, slat noise has gained the most attention in the published literature. In [77, 78, 80, 82–85, 87, 91], nearfield noise was studied, directly from the pressure signals obtained by the flow simulation. Lockard and Choudhari [81] and Ma and Zhang [89] used the FWH method to predict the farfield-noise signature. For predicting flap noise, the vortex appearing at the side of the flap should be studied, which is not possible with two-dimensional airfoil models. More complex high-lift airfoils, thus, need to be considered in the simulation of flap side noise. Yao et al. [92, 93] analyzed the farfield noise of several three-dimensional swept wings with deployed high-lift devices, based on hybrid RANS/LES flow fields.

The DLR F15 model investigated here, was also studied with turbulence-resolving simulations in terms of the flow field and nearfield noise by Terracol and Deck [85] and Deck [82]. Reuß et al. [88] additionally examined the flow field around the airfoil with a range of different global hybrid RANS/LES methods.

3.1.2 Simulations and work flow

Initially, two-dimensional precursor RANS simulations were performed to predict the pressure distribution around the airfoil and to find the corrected AoA [94]. The simulations are carried out at free flight conditions, which is a different situation than in the wind tunnel measurements, where the presence of the wind tunnel walls lead to blockage effects. The measurements were performed at an AoA of 7.05° and the blockage leads to additional flow acceleration on the suction side, indicating that the AoA should be higher in the simulations in order to account for the increased lift force. Interestingly, the corrected AoA was found to be 6° based on RANS simulations with the $k-\omega$ SST model [95] and the Peng-Davidson-Holmberg low-Reynolds-number model [96].

⁵ Implicit LES does not use a SGS model, but relies on numerical dissipation to remove the energy at high wave numbers

In the wind tunnel measurements, the location for boundary-layer transition from laminar to turbulent on each of the airfoil's elements was also determined. The regions of laminar boundary layers are indicated in blue in Fig. 3.3. It was found that correct specification of the transition locations was crucial for obtaining good results in terms of pressure distribution [94]. Boundary-layer transition is simulated by simply suppressing the turbulent viscosity (or its production) near the wall in the laminar regions.

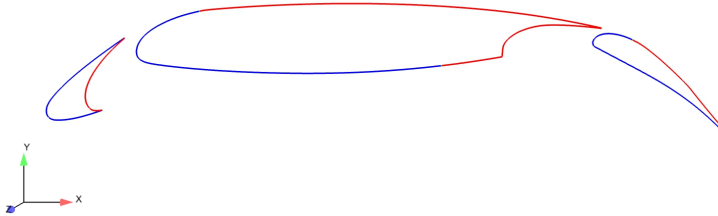


Figure 3.3: *Specified boundary-layer transition locations.* —: laminar, —: turbulent.

For the turbulence-resolving simulations, the two-dimensional airfoil was extruded in spanwise direction. Classical SADES [29] and an algebraic hybrid RANS/LES method [66, 67] were employed. The simulations started from converged RANS flow fields and were undergoing an initial phase in which resolved turbulence was developing. Once the simulations reached their quasi-steady state with fully-developed resolved turbulence content, time-averaging of the flow field was initiated. Drag and lift coefficients were monitored over time in order to decide when the fully-developed state was reached. Time histories of fluctuating flow variables were extracted during runtime for post-processing purposes at locations of interest.

In order to enable the aeroacoustic analysis, fluctuating flow-field variables were stored for a certain amount of simulation time. To save disk space, not the entire flow field was saved at each time step, but the relevant variables were stored on an integral surface in the nearfield of the airfoil. This integral surface is a permeable, closed surface, which is not seen by the flow and simply serves as a sampling surface. The placement of the surface is somewhat ambiguous and includes a certain trade-off. Theoretically, the surface needs to be far enough from the airfoil to ensure that all acoustic noise sources are enclosed within it. Obviously the probability of this being true increases when the surface is located further and further away from the wing. At the same time, the grid requirement is such that the grid needs to be fine enough to allow for propagation of sound waves from the airfoil to the surface. For surfaces placed far away from the airfoil, this may become prohibitively costly. As the location of the surface needs to be decided at the grid development stage, a-priori knowledge of the expected flow field is necessary. Here, precursor simulations with the HYB0 model were used to determine the surface location. For that purpose, the vorticity magnitude was plotted, which should give an indication of the outreach of the resolved turbulence and the surface was placed as to include the largest part of that resolved turbulence. The location of the integral surface and the grid around the airfoil's elements are shown in Fig. 3.4. Since the slat is known to be a prime

contributor to high-lift noise, main focus was put on the grid in the slat region, where the resolution should be fine enough to capture the instability in the shear layer detaching from the slat cusp and the upper slat trailing edge.

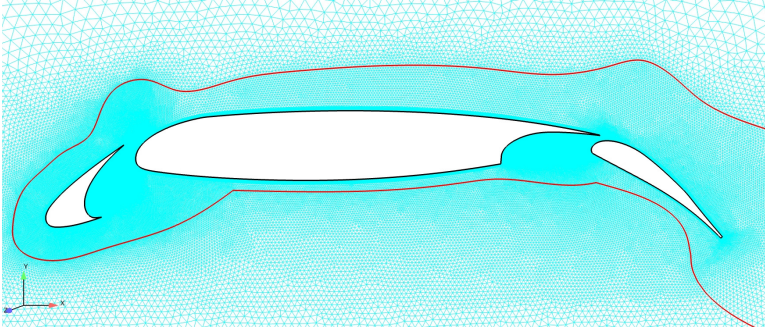


Figure 3.4: *Integral surface for noise-radiation calculations and the computational grid. The integral surface is indicated by the red, solid line surrounding the airfoil.*

Three different acoustic analogies were used for the farfield-noise prediction, namely Curle’s analogy [97], Kirchhoff’s analogy [98] and Ffowcs-Williams and Hawkings’ analogy [99, 100]. All three analogies are described in detail in Appendix A. For the Curle analogy, pressure fluctuations at the solid surface of the airfoil’s elements serve as input, while the Kirchhoff and FWH analogies rely on pressure and velocity fluctuations at the integral surface as input.

Figure 3.5 illustrates the different steps involved in the work flow of carrying out an aeroacoustic analysis based on hybrid RANS/LES simulations.

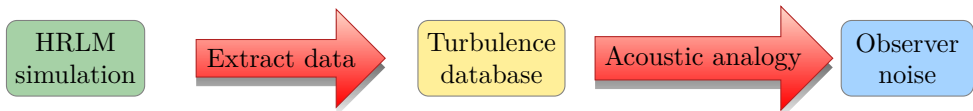


Figure 3.5: *Work flow for carrying out an aeroacoustic analysis with acoustic analogies based on input data from hybrid RANS/LES simulations.*

3.1.3 Numerical description

All computations were performed with the finite-volume solver Edge, developed by FOI (Swedish Defense Research Agency) [101, 102]. Edge solves the compressible Navier-Stokes equations on unstructured grids with arbitrary elements. The solver uses an edge-based formulation with a node-centered finite-volume technique. That implies that a dual grid is generated around the nodes of the original grid, forming the control volumes. The control volume surfaces intersect the edges of the original grid in their midpoint and the fluxes are evaluated for the control volume surfaces for each edge connected to a node. Time integration is carried out using an implicit dual time-stepping routine with explicit sub iterations. At each sub iteration, the governing equations are solved using

an explicit three-stage Runge-Kutta method. For the case considered, about 100 sub iterations were usually carried out at each time step, ensuring that the residuals decreased by at least two orders of magnitude. The implicit time-integration scheme used is the second-order accurate Euler backward scheme. To speed up solution convergence, an algebraic multigrid technique with implicit residual smoothing was employed. The spatial discretization is based on a second-order accurate central scheme with added artificial dissipation. The message passing interface (MPI) is used for parallelization of the code.

3.1.4 Typical results

As mentioned above, the flow around the high-lift airfoil is characterized by a number of interesting flow phenomena, some of which can be visualized in the flow field. Figure 3.6 shows a snapshot of the resolved turbulence structure in the slat cove and on the flap. In the slat cove, the shear layer and the re-circulation region are clearly visible and it can also be seen how the shear layer impinges on the lower slat wall. Long streamwise turbulence structures are seen on the leading edge of the flap, which rapidly become three-dimensional turbulence once they get incorporated in the separated region further downstream.

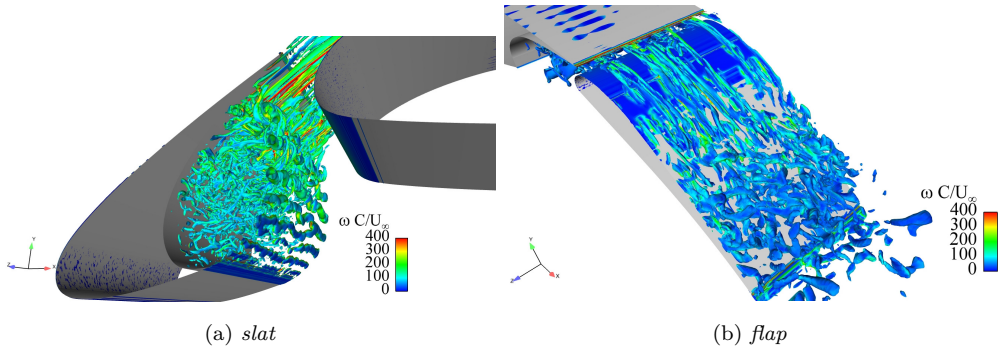


Figure 3.6: Resolved flow structures visualized by the Q -invariant. a) slat cove ($\frac{QC^2}{U_\infty^2} = 5000$, where C is the stowed chord length and U_∞ is the freestream velocity), b) flow separation on the flap ($\frac{QC^2}{U_\infty^2} = 1000$). Coloring by vorticity magnitude.

The mean flow field, including shear layers, multiple flow stagnation and re-circulation regions, as well as flow acceleration through the gaps between the airfoil's elements can be observed in Fig. 3.7. Moreover, the merging of wakes and boundary layers is visible on the leading edge of the main wing.

Figure 3.8 gives an impression of the results from the aeroacoustic simulations. In Fig. 3.8a, the sound-pressure-level (SPL) spectrum in the downward direction (towards possible observers) obtained with the three different acoustic analogies is presented, indicating similar results for the Kirchhoff and FWH analogies above a Strouhal number of approximately 1.5. Below that, clearly larger values are obtained with the Kirchhoff

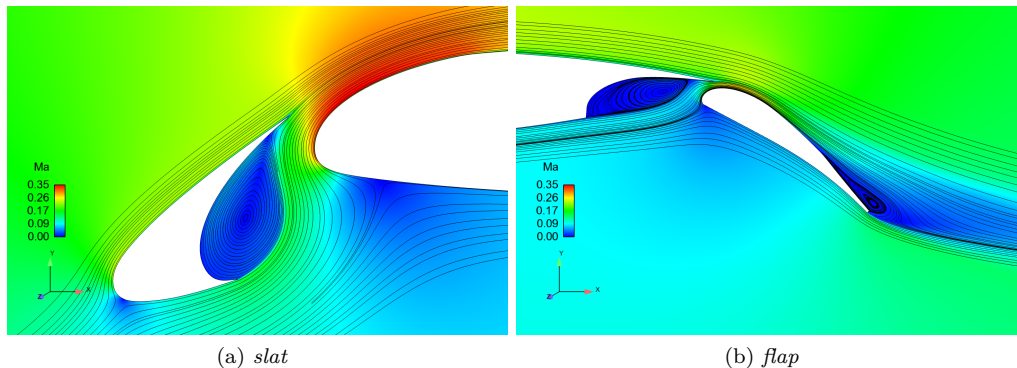


Figure 3.7: *Mean-flow pattern around the multi-element airfoil visualized by streamlines and Ma-number contours.*

method than with the other two methods. In fact, the higher values at low Strouhal numbers lead to largely increased overall SPLs (OASPL) in all directions as shown in Fig. 3.8b. The FWH and Curle analogies yield a similar shape of the directivity map, except in the downstream direction, where the FWH includes the effects of the wake and therefore yields larger noise levels. Through inclusion of volume source terms in the FWH method, the noise levels are somewhat larger than the ones obtained with Curle’s method in all directions.

3.2 Wind-turbine fatigue loads in forest regions

Owing to a multitude of advantages, placing wind turbines in forest regions is becoming an increasingly interesting possibility. As a result of the “not-in-my-backyard-attitude” of many people, it is often easier to obtain a permit for developing wind-power plants in remote regions, such as forests. Additionally, the ever increasing hub heights of new wind turbines allow for efficient operation, even in the low wind speeds typically encountered above forests. Erection, maintenance and grid connection of wind turbines are simplified in forest regions compared to offshore wind parks, due to already existing infrastructure like, for example, forestry roads. Unfortunately, the wind resource above forests is not only characterized by low wind speeds, but also by strong atmospheric turbulence and large vertical wind shear. The strong turbulence gives rise to heavy fluctuating aerodynamic loads and the wind shear will increase the cyclic loading on the wind turbine blades. Since wind turbines nowadays are not designed for usage in forest regions, one can expect that the increased fatigue loads lead to shorter maintenance interval and reduce the overall fatigue life of the wind turbine, making the wind turbines more expensive to operate. The general situation of a wind turbine in a forest is sketched in Fig. 3.9. As indicated, the wind turbine will be confronted with a wide range of different turbulent motions and a wind-speed profile with large vertical wind shear.

In order to be able to predict the effect of the forest on the fatigue life of wind

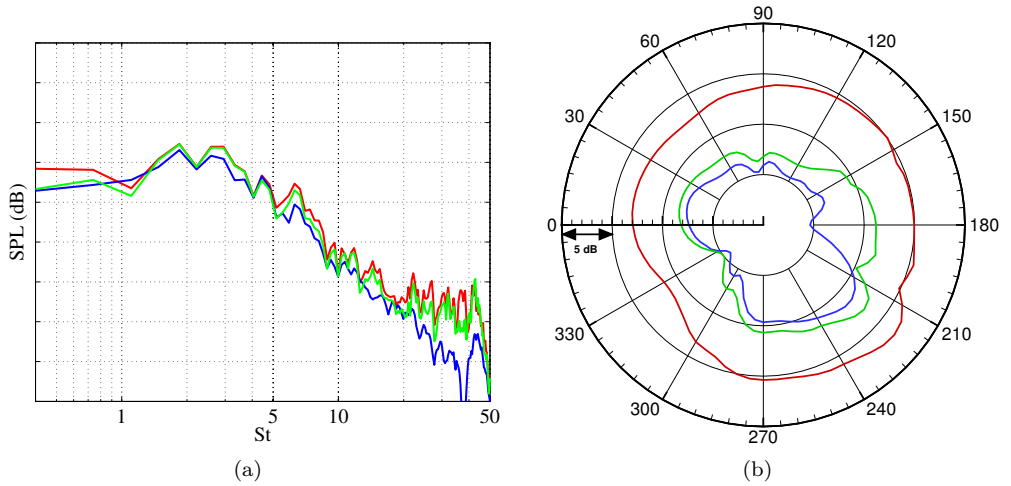


Figure 3.8: Comparison of the three different acoustic analogies. a) SPL of farfield noise in the downward direction, b) Directivity of OASPL. —: Curle's analogy, —: Kirchhoff's analogy, —: FWH's analogy

turbines, an accurate representation of the atmospheric turbulence being ingested by the wind turbine is necessary. Based on the atmospheric turbulence information, structural wind-turbine models can be used to predict the resulting fatigue loads. In industrial applications, turbulence fields are commonly synthesized from spectral models, accounting for the rather simplified turbulence characteristics required by the IEC guidelines [105]. Neutral atmospheric stability is usually assumed in spectral models, even though the ABL is rarely ever neutrally stratified and wind turbines will therefore almost always operate in non-neutral conditions. Consequently, it is sensible to include non-neutral stratification in the design process. Recently, spectral models accounting for stratification effects were proposed by Chougule et al. [106] and Segalini and Arnqvist [107]. Additionally, spectral models assume that the wind shear and the turbulence intensity are constant over the swept rotor area. As turbulence under neutral atmospheric conditions is generated mostly near the ground due to shear, the turbulence intensity generally decays with increasing height above the ground. Hence, it is questionable that the assumption of a constant turbulence intensity is valid, in particular for modern wind turbines with large rotors. Moreover, spectral models neglect the influence of the Coriolis force, which leads to wind turning with height. Large wind turbines with great hub heights may reach up into the Ekman layer of the ABL (see Section 1.2) and may therefore experience large wind veer⁶ over the swept rotor area. Furthermore, spectral models are often not fit to handle extreme roughness, such as forests. However, Chougule et al. [106] recently provided parameters to adapt the Mann model [108, 109] to forest regions, based on curve-fitting to field measurements. A comprehensive review of the simplifications and shortcomings of synthetically generated turbulence is given by Park et al. [110].

⁶ The change in wind direction with height above the ground, i.e. horizontal wind shear.

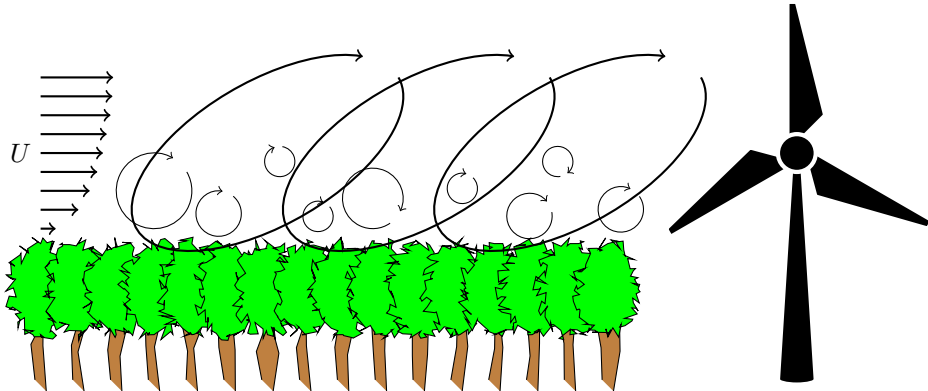


Figure 3.9: *The flow situation for a wind turbine in a forest. The mean wind-speed profile and a range of turbulent motions are shown. It is also indicated that the larger motions are more anisotropic, while the smaller ones are of a more isotropic nature (see also [103, 104]).*

One can easily imagine that a more accurate representation of the atmospheric turbulence enables more reliable predictions of the resulting wind-turbine fatigue loads. Naturally, LES can include all the above mentioned effects and subsequently, the atmospheric turbulence contained in LES flow fields should be more physically sound than the ones generated synthetically. Consequently, also the wind-turbine fatigue loads should be more accurately represented.

Proper resolution of all the boundary-layer scales on the wind-turbine blades in LES requires excessively fine grid spacing, making it infeasible to include a wind turbine explicitly in the simulation. Additional complications arise due to the usage of sliding meshes, since the wind turbine rotor should be moving to represent reality as close as possible. As a remedy, two approaches seem feasible; the wind turbine can be represented in the LES solely through the resulting torque and thrust of the rotor, as it is done in the actuator disk and line models [111–114] or the flow simulation and the fatigue-load simulation can be decoupled and performed in two subsequent steps.

Here, we chose to decouple the simulation of the flow field and the fatigue-load calculation. The Reynolds number for ABL flows is in the order of 10^7 – 10^8 , implying that we need to employ LES with a wall function for the flow simulations. From the LES, turbulence fields are extracted at each time step and are stored for later utilization as inflow turbulence for the fatigue-load simulations. The different steps involved in the work flow are detailed in Fig. 3.10.

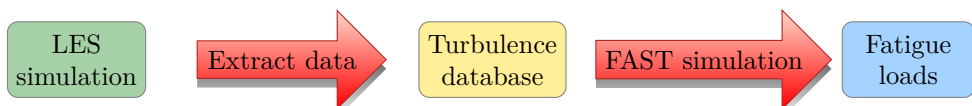


Figure 3.10: *Work flow for fatigue-load simulations of wind turbines based on inflow turbulence generated by LES.*

In the following, a short review of previous LES above and inside forests and of the application of LES for inflow turbulence generation is given. Then, the adaptation of the LES framework to the simulation of the ABL over a forest canopy along with the technique for extracting turbulence fields from the simulation is detailed. A short description of the fatigue-load simulations on a generic wind turbine, using the structural solver FAST, is also given and typical results are presented.

3.2.1 Previous work

LES has initially been developed for weather prediction purposes and has thus been intensively used for the simulation of the ABL under various thermal stratification regimes [38, 60, 115–117]. However, in these studies, the flow over forests was not considered explicitly.

The first ones to explicitly account for a forest in their LES were Shaw and Schumann [118] in 1992. They considered a horizontally homogeneous forest, parameterized through source terms in the momentum equations and accounting for the drag force exerted by the trees on the flow. Results were presented for two different canopy densities with good grid resolution ($\Delta_x = \Delta_y = \Delta_z = 2$ m) on a very restricted computational domain under neutral and unstable stratification. In 2003, Shaw and Patton [64] refined the forest model to also include the effect of skin friction of the canopy elements. Later, the influence of the density and vertical topology of horizontally homogeneous forests on the turbulence statistics were studied by Dupont and Brunet [119] and Huang et al. [120]. Simplified horizontally heterogeneous forests were investigated by Patton [121] and Yue et al. [122, 123], while also the flow over forest edges [124–129] prompted considerable research activity. Besides the mean flow and turbulence statistics, also the simulation and recognition of large coherent turbulence structures above forests is a focal point in the literature [63, 126, 130, 131]. Recently, more realistic forest features, such as randomized leaf-area densities [132] or leaf-area densities from aerial LIDAR scans [133, 134], have been implemented. Most studies have simulated forest flows under neutral or unstable stratification [62, 118, 132, 135], while stable stratification was not considered at all. Only Hu et al. [136] simulated the stable nocturnal boundary layer above a forest, but they treated the temperature field as a passive scalar.

Despite the potential of LES in providing realistic atmospheric turbulence fields, LES is to date not frequently used for the generation of inflow fields for wind-turbine fatigue-load simulations. So far, Churchfield et al. [137] have simulated wind-turbine fatigue loads directly in LES by coupling their ABL simulation to the structural wind-turbine model FAST. A two-step approach, similar to the one employed here, was chosen by Sim et al. [138] for the neutral ABL and by Park et al. [110] for the stable ABL. In all available fatigue-load studies, the ABL is simulated over flat terrain with low aerodynamic roughness. The effect of forests on the fatigue loads of wind turbines has not been assessed yet.

3.2.2 LES within and above a forest

As well-resolved LES is out of question for ABL flows due to the high Reynolds number, a wall model is commonly employed to prescribe the effects of the rough wall. Equation (2.9)

is therefore used to describe the wall-shear stress at the first vertical grid point off the wall. The aerodynamic surface roughness, z_0 , can then be adjusted to fit the desired surface texture. A list of surface-roughness values for different terrain, ranging from low-roughness surfaces, such as sand and ice, to extreme roughness, such as towns and forests, can be found in [139, 140]. Consequently, it is possible to simulate the flow over a forest, simply by increasing the surface roughness to the appropriate value. However, this approach does not account for the porosity of the forest, making it possible for the flow to enter inside the forest and even to develop secondary flows within the forest that may interact with the flow above the forest. Representing the forest similarly to a porous medium seems thus like a more adequate approach. A simple model, representing the forest through the drag force exerted by the trees on the flow, has been proposed and is widely used nowadays. The drag force is added to the filtered momentum equations (Eq. (2.6b)) as a volume source term, reading

$$F_i = -C_D a_f U \bar{u}_i, \quad (3.1)$$

where C_D is the forest drag coefficient, a_f is the leaf-area density of the forest and $U = \sqrt{\bar{u}_i \bar{u}_i}$ is the local wind speed. A wide range of values has been used for C_D , derived from field measurements [141]. In simulations, C_D is usually taken in the range of 0.15–0.2 [3, 5, 119], even though higher values of 0.26 and 0.4725 were used by Dupont et al. [127] and Finnigan et al. [130], respectively. The leaf-area density is defined as the one-sided leaf surface area per unit volume in the forest [142] and is generally unknown. It can be estimated either from empirical models, such as the one of Lalic and Mihailovic [143], from virtual canopy generators [132, 144], from tree sampling [145] or from terrestrial or aerial LIDAR scanning [133, 134].

As a consequence of the Earth’s rotation, the wind direction changes with height above ground, leading to the so-called Ekman spiral. This is caused by the Coriolis effect and should be included in the simulations through an additional source term in Eq. (2.6b).

$$F_{c,i} = 2\Omega \sin(\phi)(\bar{u}_j - u_{j,g})\varepsilon_{ij3}, \quad (3.2)$$

with Ω being the Earth’s rotation rate, $u_{j,g}$ being the geostrophic wind component, ε_{ij3} being the alternating unit tensor and ϕ being the latitude.

In order to account for thermal stratification of the ABL, the transport equation for potential temperature has to be solved.

$$\frac{\partial \bar{\theta}}{\partial t} + \frac{\partial(\bar{\theta}\bar{u}_j)}{\partial x_j} = \frac{\partial}{\partial x_j} \left(\frac{\nu}{Pr} \frac{\partial \bar{\theta}}{\partial x_j} - \tau_{i\theta} \right) + S_h, \quad (3.3)$$

where Pr is the Prandtl number, $\tau_{i\theta}$ is the SGS heat flux and S_h is the canopy heat source. Unstable conditions can be modeled through the assumption that, during the day, the forest is heated by solar radiation and that the warm forest in turn is heating the atmosphere through conduction. For the sake of simplicity, heat radiation is not usually included. The strength of the heat source is proportional to the amount of solar radiation absorbed by the vegetation. Consequently, the heat source is strongest in the upper region of the forest and diminishes with increasing depth into the canopy. Shaw

and Schumann [118] propose the following form of the canopy heat-source term,

$$S_h = \frac{\partial Q(z)}{\partial z} = \frac{\partial}{\partial z} (Q_h \exp(-\gamma A_c)), \quad (3.4)$$

where $\gamma = 0.6$ is the extinction coefficient of light [118], $Q(z)$ and Q_h are the heat-flux profile and the canopy-top heat-flux value, respectively, and $A_c = \int_z^h a_f dz$ is the downward cumulative leaf-area index, with h being the canopy height. Unstably stratified flow is then obtained by setting a positive value for Q_h . In the appended Paper E [5], it is shown that the heat source can be modeled analogously for stable conditions, i.e. by setting a negative value for Q_h , which yield a negative heat source. It should be noted, that modeling stable stratification in the same way as unstable stratification is not physically sound, since during night time, when stable conditions are most prevalent, heat transfer is largely governed by longwave radiation [146]. Measurements, however, show that the heat flux inside the canopy exhibits the largest magnitude at the canopy top in both stable and unstable stratification [11, 147, 148].

Thermal stratification of the ABL leads to buoyancy forces in the vertical component of the momentum equations. In unstable stratification, air at the bottom is warmer than the air aloft and an airparcel at the ground is therefore lighter than the airparcel above. Consequently, the lighter airparcel will rise and the heavier airparcel will move down. It can be intuitively understood that this process enhances vertical mixing. The opposite is true for stable stratification. Airparcels near the ground are colder and therefore heavier than the atmosphere aloft. Even if we displace an airparcel from the ground to higher levels, it will be heavier than the surrounding air and thus sink back to its original position. One can easily see that this process inhibits vertical mixing and dampens vertical turbulent motions. Buoyancy forces are accounted for in the vertical component of the filtered momentum equations (Eq. (2.6b)) through the term

$$F_b = \frac{g}{\theta_0} \theta'' \delta_{i3}, \quad (3.5)$$

with g being the acceleration due to gravity, θ_0 being the reference potential temperature and δ_{i3} being the Kronecker delta. The double primes denote here a deviation from the horizontal mean value.

In case the SGS model includes a transport equation for SGS turbulent kinetic energy, such as the model of Deardorff [60] described in Section 2.4.1, the destruction of SGS TKE by the forest should also be taken into account in Eq.(2.10), as

$$\varepsilon_f = -\frac{8}{3} C_D a_f U k, \quad (3.6)$$

where the factor $\frac{8}{3}$ is adapted from Shaw and Patton [64].

In the most simplified case, the terrain and the forest can be assumed to be homogeneous in the horizontal direction. That is, the ground is completely flat, there are no differences in surface roughness with horizontal position and the forest varies only in density with height. Periodic boundary conditions can then be used in the streamwise and lateral directions. Figure 3.11 illustrates the computational domain used here for LES of the

ABL over a forest canopy. The dimension of the domain in the vertical direction is usually taken to be of the order of $H \approx 1000$ m for neutral and unstable stratification, while H can be chosen smaller for the more shallow stable ABL [115]. The streamwise and lateral extent of the domain should be equal to, or larger than, the vertical dimension. Here, usually $L_x = 2H$ and $L_y = H$ were used. Bechmann [149] suggested to use lateral and streamwise domain extents of at least $3.5H$ and $6H$, respectively, for the simulation of the neutral ABL. Smaller domain extents result in wind-speed acceleration at greater heights due to the fact that large-scale turbulence is restricted by the lateral domain size.

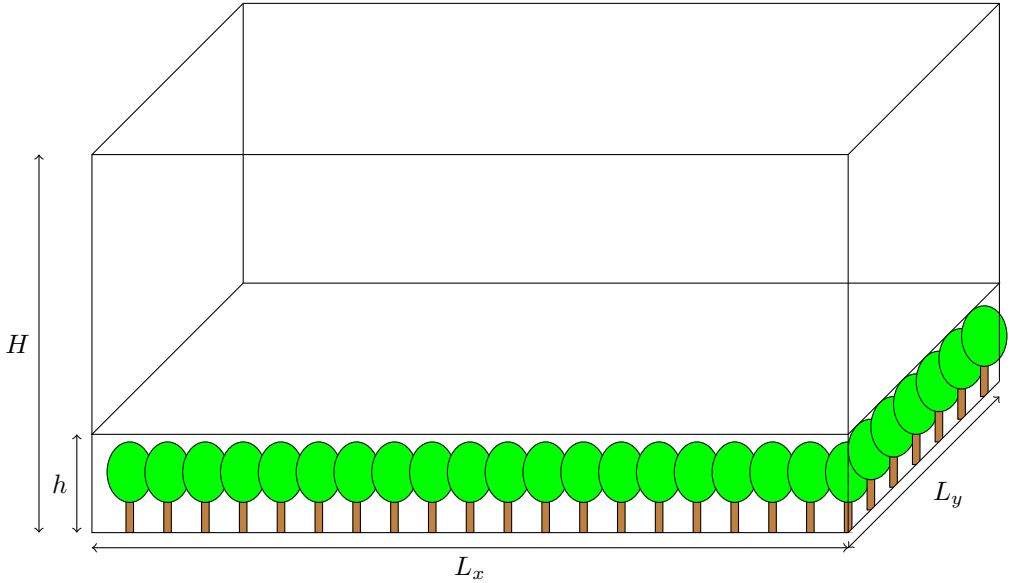


Figure 3.11: *The computational domain assuming horizontally homogeneous terrain and forest.*

Field measurement data from a test site in southeastern Sweden (Latitude 57° N) were available for validation. As mentioned by Bergström et al. [150] and Arnqvist et al. [151], the forest at the test site consisted of predominantly Scots pine trees (*pinus silvestris*) and had an average tree height of about 20 m. Following these specifications, the forest height, h , was chosen to be equal to 20 m in all of the studies. The empirical model of Lalic and Mihailovic [143] was employed to generate the leaf-area density profile shown in Fig. 3.12. The leaf-area index, $A = \int_0^h a_f dz$, of the given profile is approximately 4.3 and the profile is identical to the one used in [5]. Two examples of the canopy heat source in unstable and stable stratification are also given in Fig. 3.12. As mentioned before, the heat source is strongest in the canopy top, which is physically motivated in the unstable case, but not physically sound in the stable case.

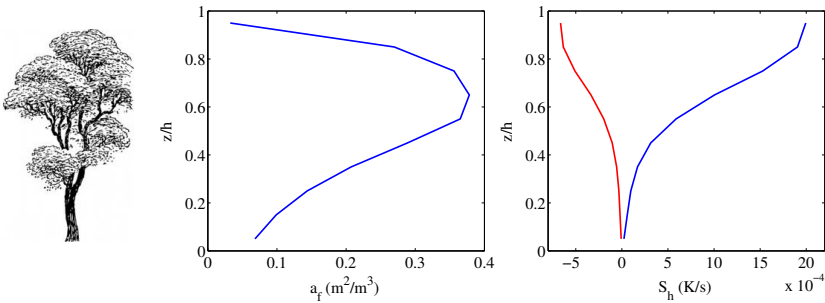


Figure 3.12: Leaf-area density, a_f (left panel) and the strength of the canopy heat flux, S_h (right panel) for a Scots pine tree. In the right panel: **—**: unstable profile, **—**: stable profile.

In the simulations, the desired flow angle and the desired mean wind speed at a reference height above ground⁷ are specified. From this information and comparison with the instantaneous flow field, the driving pressure gradient in the horizontal directions is adjusted at every time step. Assuming that the hub height of a wind turbine was chosen as the reference height, it can be assured that the extracted turbulence fields are perpendicular to the mean flow at the reference height, since the flow direction is known at that height. Subsequently, this enables performing fatigue-load simulations free from yaw angles, though the influence of wind veer is still present in the data.

Figure 3.13 shows an example of the instantaneous flow field at hub height of the NREL 5MW reference wind turbine [152]. The black lines indicate the locations of the planes used for extraction of turbulence data. Note that in total 15 sampling planes are used simultaneously in order to generate different data sets. This is possible due to the use of periodic boundary conditions and enables generation of a large amount of inflow data in reasonable CPU time. The sampling planes are quadratic in nature and their size is chosen to cover the entire swept rotor area of the wind turbine. The center of the plane is aligned with the center of the rotor and an equidistant grid is patched on the sampling plane.

3.2.3 Numerical description

All the simulations were carried out using a single-processor, incompressible, finite-volume based LES code [153]. The solver employs an implicit fractional step method. While a simple TDMA solver is used for the momentum, potential temperature and SGS kinetic energy, an efficient multigrid Poisson solver is used to solve for the pressure. A collocated grid-arrangement is used and in order to avoid pressure-velocity decoupling, the Rhie-Chow interpolation is implicitly included. The momentum equations are discretized in space using the second-order accurate central scheme, while the k -equation in the SGS model is discretized using a hybrid scheme blending between central differencing and upwinding.

⁷ It is sensible to take the hub height of the wind turbine as the reference height, but it is not a requirement.

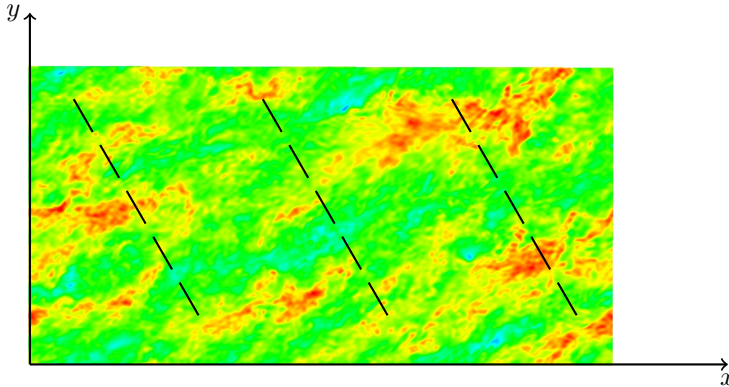


Figure 3.13: *The instantaneous flow field at the hub height and the locations of turbulence extraction planes (—)*

The potential temperature equation is treated with the van Leer scheme [154], which is a bounded second-order upwind scheme. The second-order accurate Crank-Nicolson scheme is used for time-discretization.

3.2.4 Fatigue-load simulations

For the last step of the work flow detailed in Fig. 3.10, a variety of different aeroelastic wind turbine simulators are available, including FAST [155], HAWC2 [156] and ViDyn [157, 158]. Here, mainly FAST was used, as it is open source and since there is a large user community, providing both support and validation. In Paper D, however, ViDyn was used along with an own reduced-order model.

FAST can be employed for analyzing two- or three-bladed horizontal-axis wind turbines, which can be equipped with either a downstream or an upstream rotor. Both onshore and fixed or floating offshore wind turbines can be considered. FAST uses a combined modal/multibody representation of the wind turbine in the time domain. Rigid and flexible bodies are interrelated with a number of degrees of freedom. Both the tower, the blades and the driveshaft are assumed to be flexible, while the support platform at the ground and all other components are assumed to be rigid. The tower and blades are described with the help of linear mode shapes that need to be calculated a-priori. The driveshaft is modeled as a linear torsional spring and damper. The aerodynamic forces on the rotor are evaluated through a blade-element momentum method and are based on the input flow fields from the LES. At each time step, the turbulent inflow plane is updated from the stored LES data. Collective pitch and variable-speed torque control algorithms are available for the simulation of the wind turbine dynamic response to the inflow turbulence.

Structural details of commercial wind turbines are not usually openly available and even less publishable. Hence, it can be problematic to obtain valid input parameters for the aeroelastic simulator. Commonly, information about the wind turbine blades and their composite material have to be gained in terms of reverse engineering, which

is costly and does not provide information about, for example, the wind turbine control algorithms. An alternative is to use structural information for the NREL 5MW reference wind turbine [152], which is completely openly available. The advantage being that all structural information is known and that many studies have been carried out by the community for this wind turbine already, making it easier to compare ones own results. Unfortunately, the turbine is only a concept wind turbine and no real-life prototype exists, and hence no measurement data are available for validation purposes.

Here, the NREL 5MW reference turbine in its onshore configuration was chosen for the fatigue load simulations. It is a three-bladed, horizontal-axis wind turbine with an upstream rotor orientation, delivering a rated power of 5MW. The hub height is 90 m and the blades have a length of 63 m. The structural information for the turbine is summarized in Table 3.1 and the complete structural and aerodynamical description is available in [152].

Table 3.1: Details of the NREL 5MW reference wind turbine.

Rated power	5 MW
Rotor orientation	Upstream
Number of blades	3
Cut-in wind speed	3.0 m/s
Rated wind speed	11.4 m/s
Cut-out wind speed	25.0 m/s
Cut-in rotor speed	6.9 rpm
Rated rotor speed	12.1 rpm
Rotor diameter	126 m
Hub height	90 m
Control	Collective pitch control Variable-speed torque control

3.2.5 Typical results

The instantaneous flow in the ABL is characterized by strong three-dimensional turbulence. In Fig. 3.14, the instantaneous horizontal wind speed is shown on vertical and horizontal cut-planes of the domain, for the ABL over a moderately dense forest ($A \approx 2.9$) at neutral stratification. Spatial turbulent fluctuations and large coherent turbulent motions can clearly be identified in the wind field. The horizontal cut plane is located at a vertical height of 10 m and therefore resides within the forest. One can observe that the wind speed inside the forest is generally low, but that some turbulent fluctuations are still present.

Averaging the instantaneous flow field from Fig. 3.14 in space and time yields the wind-speed profile presented in Fig. 3.15. It can be seen that good agreement with the field measurement data is achieved by the simulations. A closer look at the most relevant region of the ABL from a wind turbine's perspective is given in Fig. 3.15b. The typical features of a canopy flow, namely the strong wind-speed reduction inside of the canopy and

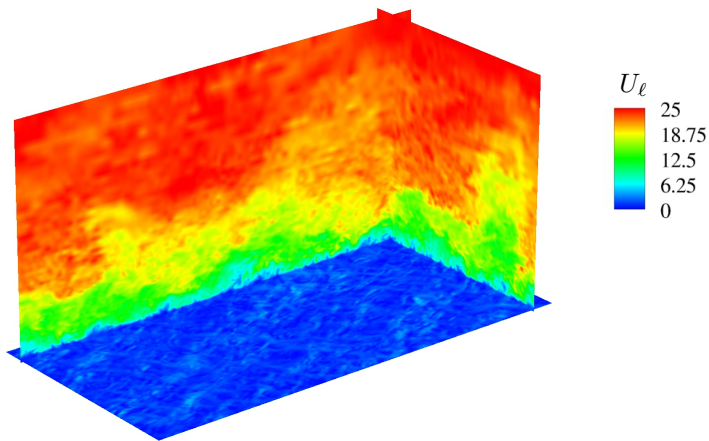


Figure 3.14: A three-dimensional snapshot of the instantaneous flow field inside and above a forest, visualized by contours of the horizontal wind speed, U_ℓ .

the inflection point at the canopy top [159, 160], are represented by the simulation results. Often, a secondary wind-speed maximum is observed deep inside the forest [161–163], but this phenomenon is not very well visible in Fig. 3.15b. However, the secondary maximum could be reported in Paper E and was found to be most pronounced in stable conditions.

A vast amount of information can be extracted from FAST. The tower-base bending moment (TBBM) was extracted for a hub-height wind speed of 12 m/s for the flows over two differently dense forests and a grass-covered landscape. Figure 3.16 depicts the power spectral density (PSD) and the mean equivalent fatigue load (EFL)⁸ obtained from averaging over 15 realizations of the fatigue-load simulations. It can be seen that the presence of a forest significantly increases the TBBM, both in terms of spectral content and in mean EFLs. The influence of the actual density of the forest appears to be small, but a higher forest density yields higher loads. As suggested by the results, the EFL of the TBBM can be expected to increase by a factor of 2.3 – 2.4 for wind turbines installed in a forest region, compared to wind turbines installed over grass-covered flat terrain.

⁸ The EFL is defined as

$$EFL = \left(\sum_{i=1}^{N_c} \frac{S_i^m}{N_0} \right)^{1/m},$$

where N_c is the number of effective load cycles, S_i are the load amplitudes, $m = 3$ is the Wöhler exponent for steel and N_0 is the equivalent number of cycles representing 10 minutes (here $N_0 = 600$ corresponding to 1 Hz). The load cycles are counted using a rainflow-counting algorithm.

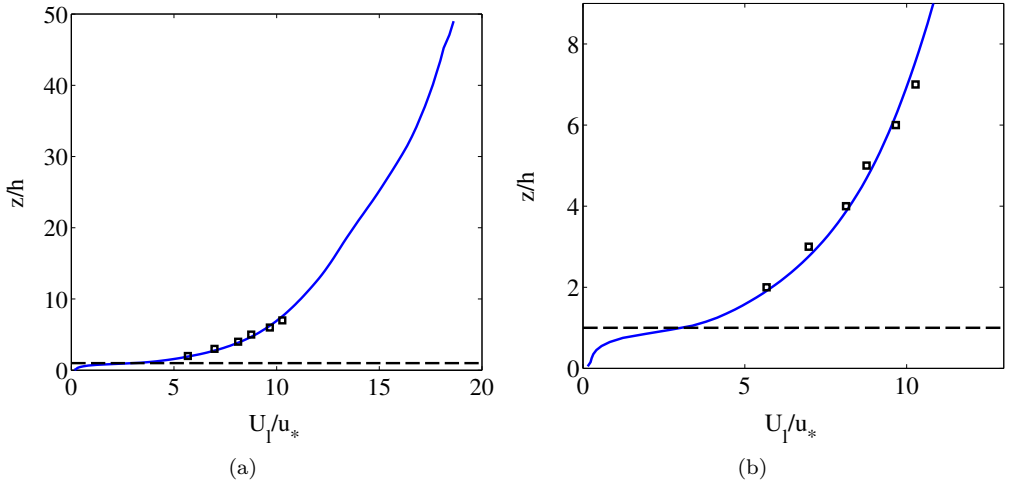


Figure 3.15: Mean wind-speed profile for a neutrally stratified ABL inside and above a dense forest ($A \approx 4.3$). a) entire domain height, b) zoom in the rotor area. —: LES, \square : Field measurements, ---: canopy top

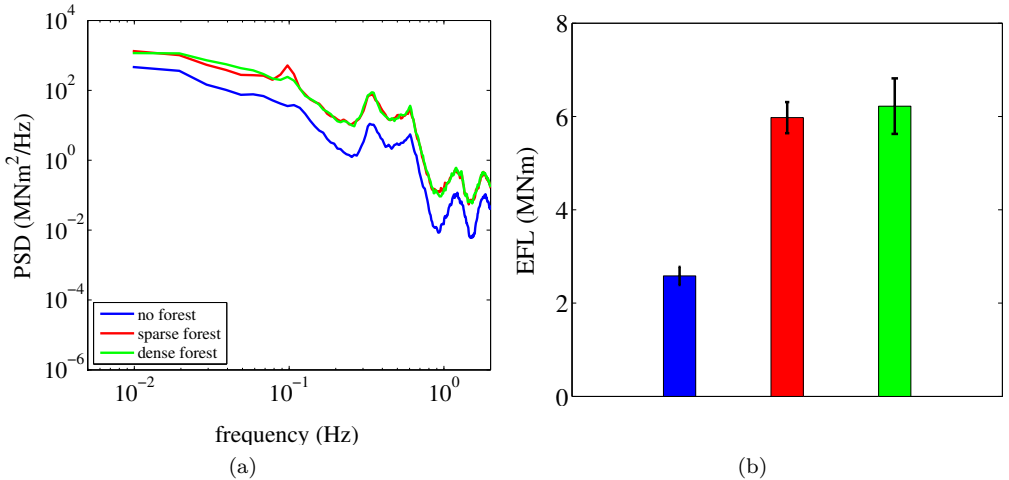


Figure 3.16: Tower-base bending moment for different forest densities at $U_{Hub} = 12$ m/s, based on 15 realizations of the fatigue-load simulations. a) PSD, b) mean EFL

4 Summary of papers

In this chapter, a brief summary of the work done and the results published in the appended papers is given. Moreover, I also critically comment on the papers and highlight what, in hindsight, should have been done differently.

4.1 Paper A

"Hybrid RANS-LES Simulation of Turbulent High-Lift Flow in Relation to Noise Generation"

4.1.1 Summary

Turbulence-resolving simulations were made for the flow around a three-element airfoil in landing configuration ($Ma = 0.15$), invoking hybrid RANS/LES methods. In order to test numerical and grid influences on the flow field, simulations were carried out using two different hybrid RANS/LES methods, at two different time steps and on grids with different spanwise domain extent. Also the nearfield noise was considered in terms of single-point spectra of the pressure fluctuations.

Both hybrid methods were able to predict reasonable mean surface-pressure distributions, compared to the experimental data. Using the smaller time step and the larger spanwise domain extent lead to improved mean pressure distributions, particularly around the slat and for the separation region at the flap. However, the shear layer forming downstream of the slat cusp showed largely delayed instability. Two-point correlations indicated that, even with the larger spanwise domain extent, pressure fluctuations were strongly correlated in spanwise direction, suggesting that even larger spanwise domains should be considered. In terms of nearfield noise, it was found that the shear-layer instability of the slat cove produces a dominant tonal peak in the sound-pressure-level spectra. Moreover, indications were found for a potential noise source at the shear-layer impingement point on the lower slat wall.

4.1.2 Comments

The results of this study lead to the conclusion that the grid should be refined for future studies, in particular in the slat cove in order to better capture the shear-layer instability. In retrospect, however, it was found that the artificial dissipation in the compressible flow solver Edge for this low Ma -number flow was probably (at least in part) responsible for the delayed onset of shear-layer instability. Owing to the low Ma number and the small temperature gradients in this case, it would have been possible to compute the flow with an incompressible solver. Using an incompressible solver with low numerical dissipation would quite likely have resulted in much improved results on the same grid. In the same way, it may be beneficial to use higher-order discretization schemes to ensure that instabilities and pressure waves are not dissipated too quickly or get polluted by numerical noise.

4.2 Paper B

"Hybrid RANS/LES Simulations for Aerodynamic and Aeroacoustic Analysis of a Multi-Element Airfoil"

4.2.1 Summary

Inspired by the previous paper, the grid around the three-element airfoil was refined. Moreover, an internal, permeable sampling surface was included in the refined grid, allowing to extract instantaneous flow-field information for post-processing purposes. The location of the sampling surface was decided a-priori, as to include all noise sources. Here, this was attempted based on the vorticity field obtained in the simulations from Paper A. The simulation was carried out using the HYB0 model described in Section 2.4.3. The sampled data were used as input for propagating the generated noise towards observer locations in the farfield, invoking three different acoustic analogies; Curle's analogy, Kirchhoff's analogy and the Ffowcs-Williams and Hawkings' analogy.

Good results in terms of mean surface-pressure distributions were obtained in the simulation and also the shear layer detaching from the slat cusp showed improved formation of instabilities, even though fully three-dimensional turbulence content was still delayed.

The aeroacoustic analysis showed good agreement of the three acoustic analogies in terms of tonal farfield noise. Using the Kirchhoff and FWH methods, a broad-banded high-frequency peak, associated with the vortex shedding from the slat trailing edge could be captured. The slat could be established as the main contributor to airframe noise in this case. Moreover, it was found that the slat and flap act as dipole noise sources and emit noise in the directions orthogonal to their own orientation.

Considerably larger noise levels were found using the Kirchhoff method, compared to the other two methods, mainly originating from Strouhal numbers below 1.5. A possible reason for this discrepancy may be that the integral surface was not placed sufficiently far from the airfoil for the Kirchhoff analogy.

4.2.2 Comments

As the acoustic analogies of Kirchhoff and Ffowcs-Williams and Hawkings assume that all noise sources are enclosed by the integral surface (sampling surface), it is a crucial step to ensure that this is true. Even though, thought was given to the location of the sampling surface, and a decision was made, based on a-priori flow fields, the paper lacks verification of this basic assumption. It would have been straightforward to include several sampling surfaces with different distances to the airfoil in the grid, which would have allowed for evaluation of the influence of the sampling-surface location. The discrepancy between the FWH and Kirchhoff method in predicted SPLs was considerable and it is speculated that the surface was not sufficiently far from the airfoil for using the Kirchhoff method. Also this speculation could have easily been proven or disproven by including several sampling surfaces.

4.3 Paper C

"Influence of a forest canopy on the neutral atmospheric boundary layer - A LES study"

4.3.1 Summary

In this paper, the influence of the presence of a forest on the neutral ABL was investigated and the possible impact for the wind-power industry was highlighted. For that purpose, results from a LES including a horizontally homogeneous forest and from a LES over flat terrain with low aerodynamic roughness were compared.

Good agreement with field measurements above a coniferous forest in southeastern Sweden was shown for the simulation including the forest canopy. It was found that the presence of the forest increased both the wind-shear exponent and the turbulence intensity at 90 m above ground (corresponding to the hub height of typical wind turbines) far beyond the wind-turbine design criteria proposed by the IEC. By means of quadrant analysis, the importance of sweeps (events carrying high-momentum air downwards) and ejections (events carrying low-momentum air upwards) could be pointed out. It was shown that the upper region of the forest is mainly penetrated by sweeps, which also become the main means of momentum transport near the ground in the without-canopy case. Plots of skewness and kurtosis indicated that strong, intermittent events occur above the forest, and that they are most likely to be sweeps. As these intermittent, extreme gusts may induce potentially harmful loads on a wind turbine, their occurrence should be taken into account in the design process.

4.3.2 Comments

This paper served as the predecessor and gave the idea for paper E. A domain height of 400 m was used here, not allowing for the simulation of the entire neutral ABL, which typically is of the order of 1000 m. The influence of neglecting the largest turbulent eddies (of the same size as the ABL) would have been interesting to investigate at this point.

4.4 Paper D

"Development of a reduced-order model for wind turbine response to atmospheric turbulence in forest regions"

4.4.1 Summary

This paper describes the development of a simple reduced-order model (ROM), including a flexible tower and a rigid, but rotating, rotor, for load calculations on wind turbines based on LES inflow turbulence. The rotor is represented as a resulting force and moment, computed with a blade-element momentum method, and applied to the top of the flexible tower. The NREL 5MW reference wind turbine is chosen for modeling. The ROM is then used with turbulence fields from LES of the ABL over a forest and over flat terrain with

low roughness. For validation purposes, the structural wind-turbine simulator ViDyn [157, 158] is also used and the results are then compared.

The mean and root-mean-square (RMS) values of the tower-base bending moment were similarly predicted by both ViDyn and the ROM. Due to the rigid blades in the ROM, allowing for an immediate response of the wind turbine to the wind field, the ROM yields considerably larger numbers of effective load cycles. Moreover, the EFL values obtained from the ROM were more than twice as large as for ViDyn.

4.4.2 Comments

A mistake in the computation of the EFL values was found after publishing this paper. Correctly computed, the EFLs are very similar for both the ROM and ViDyn. One weak point is that the study is based solely on a single representation of the flow field and the resulting loads. A more probabilistic approach with averaged results of more realizations should be carried out. Owing to its simplicity, the ROM only takes into account streamwise velocity fluctuations and therefore no yaw misalignment can be tested. Moreover, there is no variable speed or collective pitch control algorithm included in the blade-element momentum method of the ROM, which limits the model to wind speeds below rated. Furthermore, the ROM is implemented in MatLab and is based on a time-stepping algorithm, which strongly inhibits the computational performance of the model, in comparison to available models like ViDyn or FAST.

4.5 Paper E

"Large-eddy simulation study of thermally stratified canopy flow"

4.5.1 Summary

In this paper, a wide range of thermal stability classes of the ABL over a homogeneous forest were simulated using LES. There are six stability classes from unstable to very stable conditions, that were identified from field measurements in a coniferous forest in southeastern Sweden. For the first time, LES results for stably stratified flow over a forest canopy were also presented. The simulated results were validated against the field measurements for all six stability classes. Good agreement was achieved for the neutral and near-neutral simulations, while the unstable and very stable case proved to be most challenging. In fact, for the very stable case, the strong damping effect of negative buoyancy forces was found to lead to numerical oscillations and subsequent failure in the LES. Even though not physically sound, the used canopy heat-source model was found to yield adequate heat-flux and temperature distributions.

The influence of thermal stratification on the flow within and above forest canopies was then investigated in greater detail. As expected, the wind shear increased and the turbulence intensity decreased in more stable stratification. A secondary wind-speed maximum was found deep inside the canopy, and its magnitude was increasing with increasingly stable stratification. Similarly, it was shown that there exist streamwise turbulent fluctuations deep inside the forest, which do, however, not contribute to vertical

momentum transport. This type of turbulence was also found in field measurements and was termed inactive turbulence. Inactive turbulence was found to be most pronounced in unstable stratification. While in unstable stratification, the flow is in fact unstably stratified throughout the entire ABL, the existence of a weakly unstable layer of air in the lower regions of the forest could be proven in stable stratification. Moreover, resolved-scale TKE is distributed to locations deep within the forest with the help of pressure transport; more so in increasingly stable stratification.

4.5.2 Comments

All simulations in this paper were carried out on a computational domain with a height of 400 m (the same as in paper C). It has been shown that this is large enough in order to capture the entire ABL in the stable and very stable case, but for the neutral and unstable cases, larger domain heights should be considered (at least of the order of 1000 m). In general, the resolved TKE was found to be underpredicted in the simulations, which may be caused by the fact that the entire ABL is not included in the simulation, and therefore the largest eddies (of the same size as the ABL thickness) could not be resolved. Furthermore, the simulations were carried out for dry atmosphere, but it is likely that the influence of water vapor on the flow above a transpiring swedish forest is not negligible.

4.6 Paper F

"Prediction of wind turbine fatigue loads in forest regions based on turbulent LES inflow fields"

4.6.1 Summary

This paper deals with wind-turbine fatigue-load simulations based on inflow turbulence from LES simulations. In order to evaluate the influence of a forest on the wind turbine fatigue loads, three different cases were computed with varying forest densities at neutral stratification. A dense forest, a sparse forest and a simulation over a flat surface with low aerodynamic roughness were carried out and inflow turbulence for the structural wind-turbine model was extracted. The fatigue load simulations were carried out using FAST for the NREL 5MW reference wind turbine. We chose to compare the fore-aft tower-base bending moment, the flapwise blade-root bending moment and the low-speed shaft bending moment.

A comparison between synthetically generated turbulence for the Ryningsnäs measurement site and LES inflow turbulence for the same site showed good agreement in terms of spectral content of the fatigue loads. In terms of mean, RMS and EFL values, the loads predicted based on LES tended to be higher. However, whether the LES turbulence or the synthetic turbulence yield more realistic loads cannot be conclusively decided.

In the paper, we show that a forest region is clearly much more hazardous for a wind turbine in terms of fatigue loads. This seems to be mainly due to the increased turbulence intensity and the increased wind shear. For example, the presence of a forest was found

to increase the RMS and EFL values of the loads by a factor of 2.6 – 2.7. However, the actual forest density appeared to have a negligible effect on the loads.

4.6.2 Comments

The LES simulations have been carried out at neutral stratification, but as Park et al. [110] advocate, the effects of thermal stratification, i.e. increased horizontal and vertical wind shear and reduced turbulence intensity, should be considered in a future study. Ideally, simulations should be validated with load measurements on wind turbines.

5 Concluding remarks

In this work, the importance and the potential of turbulence-resolving simulation techniques have been highlighted. Two different applications of industrial relevance were considered and were treated with an appropriate simulation technique. The two cases were tackled in a multi-disciplinary way, where not only the flow solution was of interest, but results from the simulations were also used for further subsequent analysis.

Firstly, the flow around a multi-element airfoil with deployed high-lift devices was studied using hybrid RANS/LES simulation techniques. Industrial interest lies in the prediction of the emitted noise of such an airfoil, in particular in the landing phase of a flight. This has been attempted based on turbulence data sampled from the time-dependent flow solution, using three different acoustic analogies. It was found that the chosen hybrid RANS/LES methods are well-suited for prediction of the flow, yielding good agreement with the experimental data. Moreover, the acoustic analysis based on the sampled instantaneous turbulence data yields reasonable results. Careful refinement of the grid in the main focus regions, where noise generation is expected to take place and ensuring that the sampling surface encloses all turbulent noise sources, seems to be of paramount importance for successful noise predictions. Moreover, the flow solver should have low numerical dissipation and, if possible, higher-order discretization schemes should be employed in order not to dissipate flow instabilities or pollute pressure waves with numerical noise. Even though it is possible to perform noise prediction studies of complex geometries based on hybrid RANS/LES simulations, the methodology seems not ready for industrial use yet. The computational demand is still very high (weeks to months on a computing cluster) and may thus be exceeding the resources available in industry.

Secondly, the atmospheric boundary layer above and inside a forest was studied with the help of LES with a wall function. The results from this study are of great interest for the wind-power industry, which suffers from increased maintenance requirements and shortened fatigue lifetimes of wind turbines installed in forest regions. The main reason for that, are the increased wind-turbine fatigue loads caused by the stronger turbulence and the larger wind shear above forests. LES simulations were carried out for both horizontally homogeneous forests and flat terrain with low aerodynamic roughness. The results of the LES including the forest showed good agreement with field measurements and comparing the forest and non-forest situations confirmed that indeed the turbulence and vertical wind shear are increased above forests. Instantaneous turbulence information sampled from the simulations was used for calculating the fatigue loads on a generic wind turbine. It could be shown that the presence of a forest in neutral stratification increases the EFLs of the investigated loads by a factor of almost three, while the actual density of the forest was found to be of less importance. Decoupling the flow simulation from the fatigue-load prediction provides the benefit of being able to simulate the forest flow under idealized conditions, such as using periodic boundary conditions in the horizontal directions. This allows for simultaneous extraction of several turbulent inflow fields and contributes to a considerable speed-up in the generation of a turbulence database, which is important for every-day industrial use.

Simulations were also performed for non-neutrally stratified flow and particular focus was put on stable conditions and their influence on the flow within and close above the

forest, which had not been studied in the published literature before. It could be shown that simply using the canopy heat-source model with negative values of Q_h yields the desired behavior representing stable atmospheric conditions. Moreover, it could be proven that, in stable stratification, a layer of unstably stratified air exists deep within the canopy. A secondary wind-speed maximum was observed near the ground inside the canopy, which was growing stronger in stably stratified conditions.

References

- [1] B. Nebenführ, S.-H. Peng, and L. Davidson. “Hybrid RANS-LES Simulation of Turbulent High-Lift Flow in Relation to Noise Generation”. *Progress in Hybrid RANS-LES Modelling, NNFM*. Ed. by S. Fu et al. Vol. 117. Springer, 2012, pp. 303–314.
- [2] B. Nebenführ, H. Yao, S.-H. Peng, and L. Davidson. “Hybrid RANS/LES Simulations for Aerodynamic and Aeroacoustic Analysis of a Multi-Element Airfoil”. *19th AIAA/CEAS Aeroacoustics Conference*. AIAA paper 20013-2066. Berlin, Germany, 27–29 May, 2013.
- [3] B. Nebenführ and L. Davidson. “Influence of a forest canopy on the neutral atmospheric boundary layer - A LES study”. *ETMM10: 10th International ERCOFTAC Symposium on Engineering Turbulence Modelling and Measurements*. Marbella, Spain, 17–19 September, 2014.
- [4] B. Nebenführ, I. Carlén, L. Caracoglia, and L. Davidson. “Development of a reduced-order model for wind turbine response to atmospheric turbulence in forest regions”. *6th International Symposium on Computational Wind Engineering*. Hamburg, Germany, 8–12 June, 2014.
- [5] B. Nebenführ and L. Davidson. Large-eddy simulation study of thermally stratified canopy flow. *Boundary-Layer Meteorology* **156.2** (2015), pp. 253–276. DOI: 10.1007/s10546-015-0025-9.
- [6] B. Nebenführ and L. Davidson. Prediction of wind turbine fatigue loads in forest regions based on turbulent LES inflow fields. *submitted to Wind Energy* (2015).
- [7] S.-H. Peng, B. Nebenführ, and L. Davidson. “Lessons learned from hybrid RANS-LES computations of a three-element airfoil flow”. *21st AIAA Computational Fluid Dynamics Conference*. San Diego, USA, 24–27 June, 2013.
- [8] F. M. White. *Fluid Mechanics (Seventh Edition in SI Units)*. 372 pp. McGraw-Hill, 2011.
- [9] L. Davidson. *Fluid mechanics, turbulent flow and turbulence modeling*. Tech. rep. Chalmers University of Technology, Göteborg, Sweden, 2011.
- [10] S. Emeis. *Wind Energy Meteorology: Atmospheric Physics for Wind Power Generation*. Springer Science & Business Media, 2012.
- [11] J. C. Kaimal and J. J. Finnigan. *Atmospheric boundary layer flows: their structure and measurement*. Oxford University Press, 1994.
- [12] H. A. Panofsky and J. A. Dutton. *Atmospheric turbulence: models and methods for engineering applications*. John Wiley & Sons, 1984.
- [13] I. P. Castro. “Turbulent flow over rough walls”. *Advances in Turbulence XII*. Springer. 2009, pp. 381–388.
- [14] M. R. Raupach, R. A. Antonia, and S. Rajagopalan. Rough-wall turbulent boundary layers. *Applied Mechanics Reviews* **44.1** (1991), pp. 1–25.
- [15] M. W. Rotach. On the influence of the urban roughness sublayer on turbulence and dispersion. *Atmospheric Environment* **33.24** (1999), pp. 4001–4008.
- [16] E. Florens, O. Eiff, and F. Moulin. Defining the roughness sublayer and its turbulence statistics. *Experiments in Fluids* **54.4** (2013), pp. 1–15.

- [17] J. R. Holton and G. J. Hakim. *An Introduction to Dynamic Meteorology*. Vol. 88. Academic press, 2012.
- [18] E. Helgason. “Development of adjoint-based optimization methods for ducted flows in vehicles”. PhD thesis. Göteborg, Sweden: Chalmers University of Technology, 2006.
- [19] U. Piomelli and E. Balaras. Wall-layer models for large-eddy simulations. *Annual Review of Fluid Mechanics* **34.1** (2002), pp. 349–374.
- [20] M. El-Alti. “Active Flow Control for Drag Reduction of Heavy Vehicles”. PhD thesis. Göteborg, Sweden: Chalmers University of Technology, 2012.
- [21] H. E. Hafsteinnsson. “Study of Supersonic Jet Noise Reduction using LES”. PhD thesis. Göteborg, Sweden: Chalmers University of Technology, 2014.
- [22] X. Wu and P. Moin. A direct numerical simulation study on the mean velocity characteristics in turbulent pipe flow. *Journal of Fluid Mechanics* **608** (2008), pp. 81–112.
- [23] X. Wu, J. Baltzer, and R. Adrian. Direct numerical simulation of a 30R long turbulent pipe flow at $R^+ = 685$: large-and very large-scale motions. *Journal of Fluid Mechanics* **698** (2012), pp. 235–281.
- [24] H. Abe, H. Kawamura, and Y. Matsuo. Direct numerical simulation of a fully developed turbulent channel flow with respect to the Reynolds number dependence. *Journal of Fluids Engineering* **123.2** (2001), pp. 382–393.
- [25] R. D. Moser, J. Kim, and N. N. Mansour. Direct numerical simulation of turbulent channel flow up to $Re = 590$. *Physics of Fluids (1994-present)* **11.4** (1999), pp. 943–945.
- [26] P. Moin and K. Mahesh. Direct numerical simulation: a tool in turbulence research. *Annual Review of Fluid Mechanics* **30.1** (1998), pp. 539–578.
- [27] S. K. Robinson. Coherent motions in the turbulent boundary layer. *Annual Review of Fluid Mechanics* **23.1** (1991), pp. 601–639.
- [28] P. R. Spalart. Strategies for turbulence modelling and simulations. *International Journal of Fluid Flow* **21** (2000), pp. 252–263.
- [29] P. R. Spalart, W.-H. Jou, M. Strelets, and S. R. Allmaras. “Comments on the Feasibility of LES for Wings and on a Hybrid RANS/LES Approach”. *Proceedings of the First AFOSR International Conference on DNS/LES*. Ruston, USA: Greyden Press, 1997, pp. 137–147.
- [30] J. Boussinesq. *Essai sur la théorie des eaux courantes*. Vol. 2. Imprimerie nationale, 1877.
- [31] S. B. Pope. *Turbulent Flows*. Cambridge University press, 2000.
- [32] D. K. Chapman. Computational Aerodynamics Development and Outlook. *AIAA Journal* **17.12** (1979), pp. 1293–1313.
- [33] H. Choi and P. Moin. Grid-point requirements for large eddy simulation: Chapman’s estimates revisited. *Physics of Fluids (1994-present)* **24.1** (2012), p. 011702.
- [34] J. H. Ferziger and M. Peric. *Computational Methods for Fluid Dynamics*. Springer Science & Business Media, 2012.
- [35] B. Fornberg. The pseudospectral method: Comparisons with finite differences for the elastic wave equation. *Geophysics* **52.4** (1987), pp. 483–501.

- [36] A. Andren. The structure of stably stratified atmospheric boundary layers: A large-eddy simulation study. *Quarterly Journal of the Royal Meteorological Society* **121**.525 (1995), pp. 961–985.
- [37] S. Basu and F. Porté-Agel. Large-Eddy Simulation of Stably Stratified Atmospheric Boundary Layer Turbulence: A Scale-Dependent Dynamic Modeling Approach. *Journal of the Atmospheric Sciences* **63**.8 (2006), pp. 2074–2091.
- [38] C. H. Moeng. A Large-Eddy Simulation Model for the Study of Planetary Boundary-Layer Turbulence. *Journal of the Atmospheric Sciences* **41**.13 (1984), pp. 2052–2062.
- [39] F. Porté-Agel, C. Meneveau, and M. B. Parlange. A scale-dependent dynamic model for large-eddy simulation: application to a neutral atmospheric boundary layer. *Journal of Fluid Mechanics* **415** (2000), pp. 261–284.
- [40] J. C. Kok and H. van der Ven. “A high-order finite-volume method with block-structured local grid refinement”. *IDIHOM: Industrialization of High-Order Methods-A Top-Down Approach*. Springer, 2015, pp. 293–314.
- [41] Y. Morinishi, T. S. Lund, O. V. Vasilyev, and P. Moin. Fully conservative higher order finite difference schemes for incompressible flow. *Journal of Computational Physics* **143**.1 (1998), pp. 90–124.
- [42] L. Davidson and N. Andersson. Direct Numerical Simulations Using High-Order Finite Volume Methods. *submitted to Physics of Fluids* (2015).
- [43] F. R. Menter and M. Kuntz. “Adaption of eddy-viscosity turbulence models to unsteady separated flow behind vehicles”. *Symposium on the aerodynamics of heavy vehicles: trucks, buses and trains*. Ed. by R. McCallen, F. Browand, and J. Ross. Monterey, USA, 2–6 December: Springer, 2002.
- [44] F. R. Menter, M. Kuntz, and R. Langtry. “Ten Years of Industrial Experience with the SST Turbulence Model”. *Turbulence, Heat and Mass Transfer 4*. Antalya, Turkey: Begell House, 2003.
- [45] S. Deck. Numerical Simulation of Transonic Buffet over a Supercritical Airfoil. *AIAA Journal* **43** (2005), pp. 1556–1566.
- [46] P. R. Spalart, S. Deck, M. L. Shur, K. D. Squires, M. K. Strelets, and A. K. Travin. A new Version of Detached-Eddy Simulation, resistant to Ambiguous Grid Densities. *Theoretical and Computational Fluid Dynamics* **20** (2006), pp. 181–195.
- [47] M. L. Shur, P. R. Spalart, M. K. Strelets, and A. K. Travin. A hybrid RANS-LES approach with delayed-DES and wall-modelled LES capabilities. *International Journal of Heat and Fluid Flow* **29** (2008), pp. 1638–1649.
- [48] L. Davidson and S. Dahlström. Hybrid LES-RANS: an approach to make LES applicable at high Reynolds number. *International Journal of Computational Fluid Dynamics* **19** (2005), pp. 415–427.
- [49] L. Davidson and S.-H. Peng. “A hybrid LES-RANS model based on a one-equation SGS model and a two-equation $k - \omega$ model”. *Proceedings of 2nd International Symposium on Turbulence and Shear Flow Phenomena*. Ed. by E. Lindborg, A. Johansson, J. Eaton, J. Humphrey, N. Kasagi, M. Leschziner, and M. Sommerfeld. Vol. 2. Stockholm, Sweden, 2001, pp. 175–180.
- [50] P. R. Spalart. Detached-Eddy Simulation. *Annual Reviews of Fluid Mechanics* **41** (2009), pp. 181–202.

- [51] N. Chauvet, S. Deck, and L. Jacquin. Zonal detached eddy simulation of a controlled propulsive jet. *AIAA Journal* **45.10** (2007), pp. 2458–2473.
- [52] S. Deck. Recent improvements in the Zonal Detached Eddy Simulation (ZDES) formulation. *Theoretical and Computational Fluid Dynamics* (2011), pp. 1–28.
- [53] J. C. Kok and H. van der Ven. *Capturing free shear layers in hybrid RANS-LES simulations of separated flow*. Tech. rep. NLR-TP-2012-333. National Aerospace Laboratory NLR, 2012.
- [54] L. Davidson. Hybrid LES-RANS: back scatter from a scale-similarity model used as forcing. *Philosophical Transactions of the Royal Society* **367** (2009), pp. 2905–2915.
- [55] S.-H. Peng. “Hybrid RANS-LES modelling with an energy backscatter function incorporated in the LES mode”. *Turbulence, Heat and Mass Transfer 7*. Palermo, Italy, 24–27 September: Begell House, Inc., 2012.
- [56] J. Kok and H. van der Ven. “Destabilizing Free Shear Layers in X-LES Using a Stochastic Subgrid-Scale Model”. *Progress in Hybrid RANS-LES Modelling, NNFM*. Ed. by S.-H. Peng et al. Vol. 111. Springer, 2010, pp. 179–189.
- [57] L. Davidson and M. Billson. Hybrid LES-RANS using synthesized turbulent fluctuations for forcing in the interface region. *International Journal of Heat and Fluid Flow* **27** (2006), pp. 1028–1042.
- [58] T. S. Lund, X. Wu, and K. D. Squires. Generation of Turbulent Inflow Data for Spatially-Developing Boundary Layer Simulations. *Journal of Computational Physics* **140** (1998), pp. 233–258.
- [59] P. R. Spalart. Direct simulation of a turbulent boundary layer up to $R_\theta = 1410$. *Journal of Fluid Mechanics* **187** (1988), pp. 61–98.
- [60] J. W. Deardorff. Stratocumulus-capped mixed layers derived from a three-dimensional model. *Boundary-Layer Meteorology* **18.4** (1980), pp. 495–527.
- [61] M. A. Jiménez and J. Cuxart. Large-eddy simulations of the stable boundary layer using the standard Kolmogorov theory: Range of applicability. *Boundary-Layer Meteorology* **115.2** (2005), pp. 241–261.
- [62] M. J. Dwyer, E. G. Patton, and R. H. Shaw. Turbulent kinetic energy budgets from a large-eddy simulation of airflow above and within a forest canopy. *Boundary-Layer Meteorology* **84.1** (1997), pp. 23–43.
- [63] M. Kanda and M. Hino. Organized structures in developing turbulent flow within and above a plant canopy, using a large eddy simulation. *Boundary-Layer Meteorology* **68.3** (1994), pp. 237–257.
- [64] R. H. Shaw and E. G. Patton. Canopy element influences on resolved-and subgrid-scale energy within a large-eddy simulation. *Agricultural and Forest Meteorology* **115.1** (2003), pp. 5–17.
- [65] P. R. Spalart and S. R. Allmaras. A one-equation turbulence model for aerodynamic flows. *La Recherche Aéronautique* **1** (1994), pp. 5–21.
- [66] S.-H. Peng. “Hybrid RANS-LES Modeling based on Zero- and One-Equation Models for Turbulent Flow Simulation”. *Proceedings of 4th International Symposium on Turbulence and Shear Flow Phenomena*. Vol. 3. Williamsburg, USA, 27–29 June, 2005, pp. 1159–1164.

- [67] S.-H. Peng. “Algebraic Hybrid RANS-LES Modelling Applied to Incompressible and Compressible Turbulent Flows”. *36th Fluid Dynamics Conference and Exhibit*. AIAA paper 2006-3910. San Francisco, USA, 5–8 June, 2006.
- [68] J. Smagorinsky. General Circulation Experiments with the Primitive Equations I. The basic Experiment. *Monthly Weather Review* **91** (1963), pp. 99–164.
- [69] B. S. Baldwin and H. Lomax. “Thin Layer Approximation and Algebraic Model for Separated Turbulent Flows”. *16th Aerospace Sciences Meeting*. Huntsville, USA: AIAA, 1978.
- [70] I. C. A. Organization. *Annex 16 to the Convention on International Civil Aviation, Volume 1 Aircraft Noise*. 4th. ICAO. 2005.
- [71] J. Wild, M. Pott-Pollenske, and B. Nagel. “An integrated design approach for low noise exposing high-lift devices”. *3rd AIAA Flow Control Conference*. AIAA paper 2006-2843. San Francisco, USA, 5–8 June, 2006.
- [72] R. Vichnevetsky and J. B. Bowles. *Fourier analysis of numerical approximations of hyperbolic equations*. Vol. 5. Siam, 1982.
- [73] C. L. Rumsey and S. X. Ying. Prediction of high lift: review of present CFD capability. *Progress in Aerospace Sciences* **38.2** (2002), pp. 145–180.
- [74] M. R. Khorrami, M. E. Berkman, and M. Choudhari. Unsteady Flow Computations of a Slat with a Blunt Trailing Edge. *AIAA Journal* **38** (2000), pp. 2050–2058.
- [75] B. A. Singer, D. P. Lockard, and K. S. Brentner. Computational Aeroacoustic Analysis of Slat Trailing-Edge Flow. *AIAA Journal* **38** (2000), pp. 1558–1564.
- [76] M. R. Khorrami, B. A. Singer, and M. E. Berkman. Time-accurate simulations and acoustic analysis of slat free shear layer. *AIAA Journal* **40.7** (2002), pp. 1284–1291.
- [77] M. Terracol, E. Labourasse, E. Manoha, and P. Sagaut. “Numerical Simulation of the 3D Unsteady Flow in a Slat Cove for Noise Prediction”. *9th AIAA/CEAS Aeroacoustics Conference and Exhibit*. AIAA paper 2003-3110. Hilton Head, USA, 12–14 May, 2003.
- [78] M. Terracol, E. Manoha, C. Herrero, E. Labourasse, S. Redonnet, and P. Sagaut. Hybrid methods for airframe noise numerical prediction. *Theoretical and Computational Fluid Dynamics* **19** (2005), pp. 197–227.
- [79] S. Deck. Zonal-Detached-Eddy Simulation of the Flow Around a High-Lift Configuration. *AIAA Journal* **43** (2005), pp. 2372–2384.
- [80] M. M. Choudhari and M. R. Khorrami. Effect of Three-Dimensional Shear-Layer Structures on Slat Cove Unsteadiness. *AIAA Journal* **45** (2007), pp. 2174–2186.
- [81] D. P. Lockard and M. M. Choudhari. “Noise Radiation from a Leading-Edge Slat”. *15th AIAA Aeroacoustics Conference*. AIAA paper 2009-3101. Miami, USA, 11–13 May, 2009.
- [82] S. Deck and R. Laraufie. Numerical investigation of the flow dynamics past a three-element aerofoil. *Journal of Fluid Mechanics* **732** (2013), pp. 401–444.
- [83] T. Imamura, S. Enomoto, Y. Yokokawa, and K. Yamamoto. Three-dimensional unsteady flow computations around a conventional slat of high-lift devices. *AIAA Journal* **46.5** (2008), pp. 1045–1053.
- [84] S. H. Lee, J. R. Kim, Y. Bae, Y. W. Jo, and Y. J. Moon. “Computation of Slat Noise by a LES/LPCE Hybrid Method with Brinkman Penalization”. *16th AIAA/CEAS*

- Aeroacoustics Conference*. AIAA paper 2010-3839. Stockholm, Sweden, 7–9 June, 2010.
- [85] “Numerical Investigation of the Flow around a Three-Element High-Lift Airfoil Using Two Zonal Hybrid RANS/LES Methods: ZDES and NLDE”.
- [86] Q. Zhang, W. Schröder, and M. Meinke. A zonal RANS-LES method to determine the flow over a high-lift configuration. *Computers & Fluids* **39.7** (2010), pp. 1241–1253.
- [87] T. Knacke and F. Thiele. “Time-Resolved 3D Simulation of an Aircraft Wing with Deployed High-Lift System”. *Turbulence and Interactions*. Ed. by M. Deville, T.-H. Lê, and P. Sagaut. Vol. 110. Notes on Numerical Fluid Mechanics and Multidisciplinary Design. Springer, 2010, pp. 223–230.
- [88] S. Reuß, T. Knopp, and D. Schwamborn. “Hybrid RANS/LES Simulations of a Three-Element Airfoil”. *Progress in Hybrid RANS-LES Modelling, NNFM*. Ed. by S. Fu et al. Vol. 117. Springer, 2012, pp. 357–367.
- [89] Z. Ma and X. Zhang. Numerical investigation of broadband slat noise attenuation with acoustic liner treatment. *AIAA Journal* **47.12** (2009), pp. 2812–2820.
- [90] D. König, S. Koh, M. Meinke, and W. Schröder. Two-step simulation of slat noise. *Computers & Fluids* **39.3** (2010), pp. 512–524.
- [91] M. Terracol, E. Manoha, and B. Lemoine. “Investigation of the unsteady flow and noise sources generation in a slat cove: hybrid zonal RANS/LES simulation and dedicated experiment”. *20th AIAA Computational Fluid Dynamics Conference*. AIAA paper 2011-3203. Honolulu, USA, 27–30 June, 2011.
- [92] H. Yao, L.-E. Eriksson, L. Davidson, O. Grundestam, S.-H. Peng, and P. E. Eliasson. “Aeroacoustic Assessment of Conceptual Low-Noise High-Lift Wing Configurations”. *50th AIAA Aerospace Sciences Meeting incl. the New Horizons Forum and Aerospace Exposition*. AIAA paper 2012-0383. Nashville, USA, 9–12 January, 2012.
- [93] H. Yao, L. Davidson, L.-E. Eriksson, O. Grundestam, S.-H. Peng, and P. E. Eliasson. “Surface Integral Analogy Approaches to Computing Noise Generated by a 3D High-Lift Wing Configuration”. *50th AIAA Aerospace Sciences Meeting incl. the New Horizons Forum and Aerospace Exposition*. AIAA paper 2012-0386. Nashville, USA, 9–12 January, 2012.
- [94] B. Nebenführ, S.-H. Peng, and L. Davidson. *Precursor RANS computations for the F15 three-element high-lift configuration*. Tech. rep. FOI Memo 2865. Chalmers/FOI, 2011.
- [95] F. R. Menter. Two-Equation Eddy-Viscosity Turbulence Models for Engineering Applications. *AIAA Journal* **32** (1994), pp. 1598–1605.
- [96] S.-H. Peng, L. Davidson, and S. Holmberg. A Modified Low-Reynolds-Number k - ω Model for Recirculating Flows. *Journal of Fluids Engineering* **119** (1997), pp. 867–875.
- [97] N. Curle. The influence of solid boundaries upon aerodynamic sound. *Proceedings of the Royal Society of London. Series A, Mathematical and Physical Sciences* **231** (1955), pp. 505–514.
- [98] F. Farassat and M. K. Myers. Extension of Kirchhoff’s Formula to Radiation from Moving Surfaces. *Journal of Sound and Vibration* **123** (1988), pp. 451–460.

- [99] K. S. Brentner and F. Farassat. Modeling aerodynamically generated sound of helicopter rotors. *Progress in Aerospace Sciences* **39** (2003), pp. 83–120.
- [100] J. E. Ffowcs-Williams and D. L. Hawkings. Sound Generation by Turbulence and Surfaces in Arbitrary Motion. *Philosophical Transactions of the Royal Society* **264** (1969), pp. 321–342.
- [101] *Edge User Guide, Issue 5.2.0*. 2011.
- [102] *Edge Theoretical Formulation, Issue 5.2.0*. 2011.
- [103] D. Poggi, A. Porporato, L. Ridolfi, J. D. Albertson, and G. G. Katul. The effect of vegetation density on canopy sub-layer turbulence. *Boundary-Layer Meteorology* **111.3** (2004), pp. 565–587.
- [104] D. Poggi, G. Katul, and J. Albertson. Momentum transfer and turbulent kinetic energy budgets within a dense model canopy. *Boundary-Layer Meteorology* **111.3** (2004), pp. 589–614.
- [105] IEC. *Wind Turbine-Part 1: Design Requirements, IEC 61400-1*. Tech. rep. International Electrotechnical Commission, Geneva, Switzerland, 2005.
- [106] A. Chougule, J. Mann, A. Segalini, and E. Dellwik. Spectral tensor parameters for wind turbine load modeling from forested and agricultural landscapes. *Wind Energy* **18.3** (2015), pp. 469–481.
- [107] A. Segalini and J. Arnqvist. A spectral model for stably stratified turbulence. *to appear in Journal of Fluid Dynamics* (2015).
- [108] J. Mann. The spatial structure of neutral atmospheric surface-layer turbulence. *Journal of Fluid Mechanics* **273.1** (1994), pp. 141–168.
- [109] J. Mann. Wind field simulation. *Probabilistic Engineering Mechanics* **13.4** (1998), pp. 269–282.
- [110] J. Park, S. Basu, and L. Manuel. Large-eddy simulation of stable boundary layer turbulence and estimation of associated wind turbine loads. *Wind Energy* **17.3** (2014), pp. 359–384.
- [111] M. Calaf, C. Meneveau, and J. Meyers. Large eddy simulation study of fully developed wind-turbine array boundary layers. *Physics of Fluids (1994-present)* **22.1** (2010), p. 015110.
- [112] S. Ivanell, J. N. Sørensen, R. Mikkelsen, and D. Henningson. Analysis of numerically generated wake structures. *Wind Energy* **12.1** (2009), pp. 63–80.
- [113] N. Troldborg, G. C. Larsen, H. A. Madsen, K. S. Hansen, J. N. Sørensen, and R. Mikkelsen. Numerical simulations of wake interaction between two wind turbines at various inflow conditions. *Wind Energy* **14.7** (2011), pp. 859–876.
- [114] Y.-T. Wu and F. Porté-Agel. Large-eddy simulation of wind-turbine wakes: evaluation of turbine parametrisations. *Boundary-Layer Meteorology* **138.3** (2011), pp. 345–366.
- [115] R. J. Beare, M. K. Macvean, A. A. Holtslag, J. Cuxart, I. Esau, J.-C. Golaz, M. A. Jimenez, M. Khairoutdinov, B. Kosovic, D. Lewellen, et al. An intercomparison of large-eddy simulations of the stable boundary layer. *Boundary-Layer Meteorology* **118.2** (2006), pp. 247–272.
- [116] J. W. Deardorff. Numerical investigation of neutral and unstable planetary boundary layers. *Journal of the Atmospheric Sciences* **29.1** (1972), pp. 91–115.

- [117] R. Stoll and F. Porté-Agel. Dynamic subgrid-scale models for momentum and scalar fluxes in large-eddy simulations of neutrally stratified atmospheric boundary layers over heterogeneous terrain. *Water Resources Research* **42.1** (2006), W01409.
- [118] R. H. Shaw and U. Schumann. Large-Eddy Simulation of Turbulent Flow above and within a Forest. *Boundary-Layer Meteorology* **61.1-2** (1992), pp. 47–64.
- [119] S. Dupont and Y. Brunet. Influence of foliar density profile on canopy flow: A large-eddy simulation study. *Agricultural and Forest Meteorology* **148.6** (2008), pp. 976–990.
- [120] J. Huang, M. Cassiani, and J. D. Albertson. The effects of vegetation density on coherent turbulent structures within the canopy sublayer: a large-eddy simulation study. *Boundary-Layer Meteorology* **133.2** (2009), pp. 253–275.
- [121] E. G. Patton. “Large-eddy simulation of turbulent flow above and within a plant canopy”. PhD thesis. Davis, USA: Univeristy of California Davis, 1997.
- [122] W. Yue, C. Meneveau, M. B. Parlange, W. Zhu, R. van Hout, and J. Katz. A comparative quadrant analysis of turbulence in a plant canopy. *Water Resources Research* **43.5** (2007).
- [123] W. Yue, M. B. Parlange, C. Meneveau, W. Zhu, R. van Hout, and J. Katz. Large-eddy simulation of plant canopy flows using plant-scale representation. *Boundary-Layer Meteorology* **124.2** (2007), pp. 183–203.
- [124] M. Cassiani, G. G. Katul, and J. D. Albertson. The effects of canopy leaf area index on airflow across forest edges: large-eddy simulation and analytical results. *Boundary-Layer Meteorology* **126.3** (2008), pp. 433–460.
- [125] S. Dupont and Y. Brunet. Edge flow and canopy structure: A large-eddy simulation study. *Boundary-Layer Meteorology* **126.1** (2008), pp. 51–71.
- [126] S. Dupont and Y. Brunet. Coherent structures in canopy edge flow: A large-eddy simulation study. *Journal of Fluid Mechanics* **630** (2009), pp. 93–128.
- [127] S. Dupont, J. M. Bonnefond, M. R. Irvine, E. Lamaud, and Y. Brunet. Long-distance edge effects in a pine forest with a deep and sparse trunk space: In situ and numerical experiments. *Agricultural and Forest Meteorology* **151.3** (2011), pp. 328–344.
- [128] B. Yang, R. H. Shaw, and K. T. Paw U. Wind loading on trees across a forest edge: a large eddy simulation. *Agricultural and Forest Meteorology* **141.2** (2006), pp. 133–146.
- [129] B. Yang, A. P. Morse, and K. T. Shaw R H Paw U. Large-eddy simulation of turbulent flow across a forest edge. Part II: momentum and turbulent kinetic energy budgets. *Boundary-Layer Meteorology* **121.3** (2006), pp. 433–457.
- [130] J. J. Finnigan, R. H. Shaw, and E. G. Patton. Turbulence structure above a vegetation canopy. *Journal of Fluid Mechanics* **637** (2009), pp. 387–424.
- [131] T. Watanabe. Large-eddy simulation of coherent turbulence structures associated with scalar ramps over plant canopies. *Boundary-Layer Meteorology* **112.2** (2004), pp. 307–341.
- [132] G. Bohrer, G. G. Katul, R. L. Walko, and R. Avissar. Exploring the effects of microscale structural heterogeneity of forest canopies using large-eddy simulations. *Boundary-Layer Meteorology* **132.3** (2009), pp. 351–382.

- [133] L.-É. Boudreault, A. Bechmann, L. Tarvainen, L. Klemedtsson, I. Shendryk, and E. Dellwik. A LiDAR method of canopy structure retrieval for wind modeling of heterogeneous forests. *Agricultural and Forest Meteorology* **201** (2015), pp. 86–97.
- [134] F. Schlegel, J. Stiller, A. Bienert, H.-G. Maas, R. Queck, and C. Bernhofer. Large-eddy simulation of inhomogeneous canopy flows using high resolution terrestrial laser scanning data. *Boundary-Layer Meteorology* **142.2** (2012), pp. 223–243.
- [135] S. Shen and M. Y. Leclerc. Modelling the turbulence structure in the canopy layer. *Agricultural and Forest Meteorology* **87.1** (1997), pp. 3–25.
- [136] X. Hu, X. Lee, D. E. Stevens, and R. B. Smith. A Numerical Study of Nocturnal Wavelike Motion in Forests. *Boundary-Layer Meteorology* **102.2** (2002), pp. 199–223.
- [137] M. J. Churchfield, S. Lee, J. Michalakes, and P. J. Moriarty. A numerical study of the effects of atmospheric and wake turbulence on wind turbine dynamics. *Journal of Turbulence* **13** (2012).
- [138] C. Sim, S. Basu, and L. Manuel. On space-time resolution of inflow representations for wind turbine loads analysis. *Energies* **5.7** (2012), pp. 2071–2092.
- [139] J. Wieringa. Updating the Davenport roughness classification. *Journal of Wind Engineering & Industrial Aerodynamics* **41.1** (1992), pp. 357–368.
- [140] J. Wieringa. Representative roughness parameters for homogeneous terrain. *Boundary-Layer Meteorology* **63.4** (1993), pp. 323–363.
- [141] R. H. Shaw, G. Den Hartog, and H. H. Neumann. Influence of foliar density and thermal stability on profiles of Reynolds stress and turbulence intensity in a deciduous forest. *Boundary-Layer Meteorology* **45.4** (1988), pp. 391–409.
- [142] R. B. Myneni, J. Ross, and G. Asrar. A review on the theory of photon transport in leaf canopies. *Agricultural and Forest Meteorology* **45.1** (1989), pp. 1–153.
- [143] B. Lalic and D. T. Mihailovic. An Empirical Relation Describing Leaf-Area Density inside the Forest for Environmental Modeling. *Journal of Applied Meteorology* **43.4** (2004).
- [144] G. Bohrer, M. Wolosin, R. Brady, and R. Avissar. A virtual canopy generator (V-CaGe) for modelling complex heterogeneous forest canopies at high resolution. *Tellus B* **59.3** (2007), pp. 566–576.
- [145] D. B. Clark, P. C. Olivas, S. F. Oberbauer, D. A. Clark, and M. G. Ryan. First direct landscape-scale measurement of tropical rain forest Leaf Area Index, a key driver of global primary productivity. *Ecology Letters* **11.2** (2008), pp. 163–172.
- [146] J. R. Garratt. *The atmospheric boundary layer*. 316 pp. Cambridge University Press, 1992.
- [147] D. Cava, G. G. Katul, A. Scrimieri, D. Poggi, A. Cescatti, and U. Giostra. Buoyancy and the sensible heat flux budget within dense canopies. *Boundary-Layer Meteorology* **118.1** (2006), pp. 217–240.
- [148] S. Dupont and E. G. Patton. Influence of stability and seasonal canopy changes on micrometeorology within and above an orchard canopy: The CHATS experiment. *Agricultural and Forest Meteorology* **157** (2012), pp. 11–29.
- [149] A. Bechmann. “Large-Eddy Simulation of Atmospheric Flow over Complex”. PhD thesis. Roskilde, Denmark: Technical University of Denmark, Risø National Laboratory, Nov. 2006.

- [150] H. Bergström, H. Alfredsson, J. Arnvist, I. Carlén, E. Dellwik, J. Fransson, H. Ganander, M. Mohr, A. Segalini, and S. Söderberg. *Wind Power in Forests: Wind and Effects on Loads*. Tech. rep. Vindforsk Rapport, Elforsk AB, 2013.
- [151] J. Arnvist, E. Dellwik, A. Segalini, and H. Bergström. Wind Statistics from a Forested Landscape. *Boundary-Layer Meteorology* **156.1** (2015), pp. 53–71.
- [152] J. M. Jonkman, S. Butterfield, W. Musial, and G. Scott. *Definition of a 5-MW reference wind turbine for offshore system development*. National Renewable Energy Laboratory Golden, CO, 2009.
- [153] L. Davidson and S.-H. Peng. Hybrid LES-RANS modelling: a one-equation SGS model combined with $ak-\omega$ model for predicting recirculating flows. *International Journal for Numerical Methods in Fluids* **43.9** (2003), pp. 1003–1018.
- [154] B. Van Leer. Towards the ultimate conservative difference scheme. II. Monotonicity and conservation combined in a second-order scheme. *Journal of Computational Physics* **14.4** (1974), pp. 361–370.
- [155] J. M. Jonkman and M. L. Buhl Jr. *FAST User’s Guide*. Tech. rep. NREL/EL-500-29798. Golden, Colorado: National Renewable Energy Laboratory, 2005, 2005.
- [156] T. J. Larsen and A. M. Hansen. *How 2 HAWC2, the user’s manual*. Tech. rep. Risø National Laboratory, 2007.
- [157] H. Ganander and O. B. *ViDyn: Simulation program for horizontal axis windpower plants*. Tech. rep. Teknikgruppen AB, Stockholm, Sweden, 1998.
- [158] H. Ganander. The Use of a Code-generating System for the Derivation of the Equations for Wind Turbine Dynamics. *Wind Energy* **6.4** (2003), pp. 333–345.
- [159] J. J. Finnigan. Turbulence in plant canopies. *Annual Review of Fluid Mechanics* **32.1** (2000), pp. 519–571.
- [160] M. R. Raupach, J. J. Finnigan, and Y. Brunet. Coherent eddies and turbulence in vegetation canopies: the mixing-layer analogy. *Boundary-Layer Meteorology* **78.3-4** (1996), pp. 351–382.
- [161] D. D. Baldocchi and T. P. Meyers. Turbulence structure in a deciduous forest. *Boundary-Layer Meteorology* **43.4** (1988), pp. 345–364.
- [162] S. Launiainen, T. Vesala, M. Mölder, I. Mammarella, S. Smolander, Ü. Rannik, P. Kolari, P. Hari, A. Lindroth, and G. G. Katul. Vertical variability and effect of stability on turbulence characteristics down to the floor of a pine forest. *Tellus B* **59.5** (2007), pp. 919–936.
- [163] H. B. Su, H. P. Schmid, C. S. Vogel, and P. S. Curtis. Effects of canopy morphology and thermal stability on mean flow and turbulence statistics observed inside a mixed hardwood forest. *Agricultural and Forest Meteorology* **148.6** (2008), pp. 862–882.
- [164] B. Basara, S. Krajnovic, and S. Girimaji. “PANS vs. LES for computations of the flow around a 3D bluff body”. *ETMM7: 7th International ERCOFTAC Symposium on Engineering Turbulence Modelling and Measurements*. Limassol, Cyprus, 4–6 June, 2008.
- [165] K. S. Brentner and F. Farassat. An Analytical Comparison of the Acoustic Analogy and Kirchhoff Formulation for Moving Surfaces. *AIAA Journal* **336** (1998), pp. 1379–1386.

- [166] L. Davidson and S.-H. Peng. “Embedded LES using PANS”. *6th AIAA Theoretical Fluid Mechanics Conference*. AIAA paper 2011-3108. Honolulu, USA, 27–30 June, 2011.
- [167] L. Davidson. “A New Approach of Zonal Hybrid RANS-LES Based on a Two-Equation k - ε Model”. *ETMM9: 9th International ERCOFTAC Symposium on Engineering Turbulence Modelling and Measurements*. Thessaloniki, Greece, 6–8 June, 2012.
- [168] L. Davidson. “Backscatter from a scale-similarity model: embedded LES of channel flow, developing boundary layer flow and backstep flow”. *8th International Symposium on turbulence and shear flow phenomena (TSFP8)*. 2013.
- [169] M. Germano, U. Piomelli, P. Moin, and W. H. Cabot. A Dynamic Subgrid-Scale Eddy Viscosity Model. *Physics of Fluids A: Fluid Dynamics* **3.7** (1991), pp. 1760–1765.
- [170] S. S. Girimaji. Partially-Averaged Navier-Stokes Model for Turbulence: A Reynolds-Averaged Navier-Stokes to Direct Numerical Simulation Bridging Method. *Journal of Applied Mechanics* **73** (2006), pp. 652–669.
- [171] A. Jimenez, A. Crespo, E. Migoya, and J. Garcia. “Advances in large-eddy simulation of a wind turbine wake”. *Journal of Physics: Conference Series*. Vol. 75. 1. IOP Publishing. 2007, p. 012041.
- [172] G. Kirchhoff. Zur Theorie der Lichtstrahlen. *Annalen der Physik* **254** (1883), pp. 663–695.
- [173] J. C. Kok. A high-order low-dispersion symmetry-preserving finite-volume method for compressible flow on curvilinear grids. *Journal of Computational Physics* **228.18** (2009), pp. 6811–6832.
- [174] E. Labourasse and P. Sagaut. Reconstruction of Turbulent Fluctuations Using a Hybrid RANS/LES Approach. *Journal of Computational Physics* **182** (2002), pp. 301–336.
- [175] M. J. Lighthill. On Sound Generated Aerodynamically. I. General Theory. *Proceedings of the Royal Society of London. Series A, Mathematical and Physical Sciences* **211** (1952), pp. 564–587.
- [176] M. J. Lighthill. On Sound Generated Aerodynamically. II. Turbulence As A Source Of Sound. *Proceedings of the Royal Society of London. Series A, Mathematical and Physical Sciences* **222** (1954), pp. 1–32.
- [177] A. S. Lyrintzis. Review: The Use of Kirchhoff’s Method in Computational Aeroacoustics. *Journal of Fluids Engineering* **116** (1994), pp. 665–676.
- [178] J. M. Ma, S.-H. Peng, L. Davidson, and F. J. Wang. A Low Reynolds Number Variant of Partially-Averaged Navier-Stokes Model for Turbulence. *International Journal of Heat and Fluid Flow* **32** (2011), pp. 413–421.
- [179] P. J. Mason. Large-eddy simulation of the convective atmospheric boundary layer. *Journal of the Atmospheric Sciences* **46.11** (1989), pp. 1492–1516.
- [180] F. Menter and Y. Egorov. “A Scale Adaptive Simulation Model using Two-Equation Models”. *43rd AIAA Aerospace Sciences Meeting and Exhibit*. AIAA paper 2005-1095. Reno, Nevada, USA, 10–13 January, 2005.

- [181] F. R. Menter, J. Schütze, and M. Gritskevich. “Global vs. Zonal Approaches in Hybrid RANS-LES Turbulence Modeling”. *Progress in Hybrid RANS-LES Modelling, NNFM*. Ed. by S. F. et al. Vol. 117. Springer, 2012.
- [182] R. Mikkelsen. “Actuator Disc Methods Applied to Wind Turbines”. PhD thesis. Lyngby, Denmark: Technical University of Denmark, June 2003.
- [183] P. J. Morris, L. N. Long, A. Bangalore, and Q. Wang. A Parallel Three-Dimensional Computational Aeroacoustics Method Using Nonlinear Disturbance Equations. *Journal of Computational Physics* **133** (1997), pp. 56–74.
- [184] B. Nebenführ. *Aerodynamic and Aeroacoustic Analysis of a Multi-Element Airfoil using Hybrid RANS/LES Modeling Approaches*. Department of Applied Mechanics, Division of Fluid Dynamics, Chalmers University of Technology, 2012.
- [185] S. A. Orszag. Numerical Methods for the Simulation of Turbulence. *Physics of Fluids (1958-1988)* **12.12** (1969), pp. 250–257.
- [186] F. Porté-Agel. A scale-dependent dynamic model for scalar transport in large-eddy simulations of the atmospheric boundary layer. *Boundary-Layer Meteorology* **112.1** (2004), pp. 81–105.
- [187] W. C. Reynolds. “The Potential and Limitations of Direct and Large Eddy Simulations”. *Whither turbulence? Turbulence at the crossroads*. Springer, 1990, pp. 313–343.
- [188] M. L. Shur, P. R. Spalart, and M. K. Strelets. Noise prediction for increasingly complex jets. Part I: Methods and tests. *International Journal of Aeroacoustics* **4** (2005), pp. 213–246.
- [189] J. N. Sørensen and W. Z. Shen. Numerical modeling of wind turbine wakes. *Journal of Fluids Engineering* **124.2** (2002), pp. 393–399.
- [190] R. Stoll and F. Porté-Agel. Large-eddy simulation of the stable atmospheric boundary layer using dynamic models with different averaging schemes. *Boundary-Layer Meteorology* **126.1** (2008), pp. 1–28.
- [191] J. Wild, G. Wichmann, F. Haucke, I. Peltzer, and P. Scholz. “Large scale separation flow control experiments within the German Flow Control Network”. *47th AIAA Aerospace Sciences Meeting including The New Horizons Forum and Aerospace Exposition*. AIAA paper 2009-530. Orlando, USA, 5–8 January, 2009.

A Aeroacoustic analogies

In the following, the three acoustic analogies used for predicting the farfield noise of the multi-element airfoil are described.

A.1 Kirchhoff surface integral method

As early as 1883, Kirchhoff's theory was published, originally intended for the description of electromagnetic waves [172]. Later on, Kirchhoff's formula has been exploited for acoustic problems on stationary and moving integral surfaces [98]. In the Kirchhoff surface integral method, a permeable control surface is assumed to enclose all acoustic noise sources. While all non-linear effects of the acoustic sources are found within the surface, outside of the surface, the flow satisfies the linear condition so that the homogeneous wave equation is fulfilled,

$$\frac{1}{c_0^2} \frac{\partial^2 p'}{\partial t^2} - \nabla^2 p' \equiv \square^2 p'(\vec{x}, t) = 0, \quad (\text{A.1})$$

where \square^2 is referred to as the wave operator. Now, the pressure in Eq. (A.1) is replaced by a discontinuous function, such that it exists outside of the surface, whereas it is set to zero inside the surface. With the help of generalized derivatives [98, 99], the generalized wave equation for the discontinuous pressure can be written as the Kirchhoff equation for a stationary surface [177],

$$\bar{\square}^2 p'(\vec{x}, t) = -\frac{\partial p'}{\partial n} \delta(f) - \frac{\partial}{\partial x_i} [p' n_i \delta(f)], \quad (\text{A.2})$$

where generalized derivatives are denoted by an overbar, as in $\bar{\square}^2$, $\delta(f)$ is the Dirac delta function, f denotes the surface and n_i denotes the components of the unit normal vector pointing outwards from the surface. A solution to Eq. (A.2) can be found via the free space Green function as

$$p'_K(\vec{x}, t) = \frac{1}{4\pi} \int_{f=0} \left(\frac{\cos \theta}{R^2} [p'(\vec{y}, t)]_\tau - \frac{1}{R} \left[\frac{\partial p'(\vec{y}, t)}{\partial n} \right]_\tau + \frac{\cos \theta}{c_0 R} \left[\frac{\partial p'(\vec{y}, t)}{\partial \tau} \right]_\tau \right) dS, \quad (\text{A.3})$$

where R denotes the distance to the observer, i.e. $R = |\vec{r}| = |\vec{x} - \vec{y}|$, $\cos \theta = (r_i/R)n_i$, c_0 is the speed of sound and $[\]_\tau$ indicates that the term is evaluated at retarded time, $\tau = t - R/c_0$. Yao et al. [93] propose to treat the three terms of Eq. (A.4) as individual

surface integrals,

$$p'_{1,K}(\vec{x}, t) = \frac{1}{4\pi} \int_{f=0} \left(\frac{\cos \theta}{R^2} [p'(\vec{y}, t)]_{\tau} \right) dS, \quad (\text{A.4a})$$

$$p'_{2,K}(\vec{x}, t) = -\frac{1}{4\pi} \int_{f=0} \left(\frac{1}{R} \left[\frac{\partial p'(\vec{y}, t)}{\partial n} \right]_{\tau} \right) dS, \quad (\text{A.4b})$$

$$p'_{3,K}(\vec{x}, t) = \frac{1}{4\pi} \int_{f=0} \left(\frac{\cos \theta}{c_0 R} \left[\frac{\partial p'(\vec{y}, t)}{\partial \tau} \right]_{\tau} \right) dS. \quad (\text{A.4c})$$

The three terms represent the noise due to pressure fluctuations, the gradient and the time derivative of the pressure fluctuations, respectively. It is, of course, still true that the total noise is the summation of the terms in Eq. (A.4), viz,

$$p'_{total,K} = p'_{1,K} + p'_{2,K} + p'_{3,K}. \quad (\text{A.5})$$

Particular care has to be taken when positioning the control surface in the domain. Since all acoustical sources have to be contained within the surface, so that the remainder of the flow field satisfies the homogeneous wave equation, the surface has to be located sufficiently far from the solid walls causing the disturbances. At the same time, CFD is used for predicting the flow field inside the surface. Due to the accuracy requirements of the CFD approach, it might not be affordable in terms of computational power, to place the Kirchhoff surface sufficiently far from the geometry. It should further be noted that different surfaces placed well outside the non-linear region of the flow should, theoretically, provide identical results [177].

A.2 Ffowcs-Williams and Hawkings' analogy

The acoustic analogy developed by Ffowcs-Williams and Hawkings [100] was derived for solid surfaces moving at an arbitrary speed, v_n . Traditionally, the surface was assumed to be impermeable and to coincide with the solid wall of the geometry. Brentner and Farassat [99] derived a formulation of the FWH analogy for a permeable surface enclosing the acoustic sources, which made the approach similar to a Kirchhoff formulation. It is shown later that this is a fundamental advantage over the original formulation, because the volume integral, accounting for the quadrupole sources in the flow, can be neglected. Here, the special case of a stationary permeable surface is used, which can easily be extracted from Brentner's formulation [99] by setting $v_n = 0$.

Brentner and Farassat [99] rewrote the compressible Navier-Stokes equations with the help of generalized functions into a generalized wave equation with non-zero source terms, which is also referred to as the FWH equation,

$$\begin{aligned} \bar{\square}^2 p'(\vec{x}, t) = & -\frac{\partial}{\partial x_i} [(p' \delta_{ij} + \rho u_i u_j) n_j \delta(f)] \\ & + \frac{\partial}{\partial t} [\rho u_j n_j \delta(f)] \\ & + \frac{\bar{\partial}^2}{\partial x_i x_j} [T_{ij} H(f)]. \end{aligned} \quad (\text{A.6})$$

In the above equation, $T_{ij} = [(p' - \rho' c_0^2)\delta_{ij} - \tau_{ij} + \rho u_i u_j]$ is the Lighthill tensor [175, 176], δ_{ij} is the Kronecker delta and $H(f)$ is the Heaviside function. Acoustical sources enclosed by the surface contribute to the sound only through the surface terms (first and second term on the right-hand side of Eq. (A.6)). The third term in Eq. (A.6) is a volume term, which accounts for sources outside the surface. It was described earlier, that when using the Kirchhoff method, we assume the surface to enclose the entire core flow region and hence all acoustical sources. Owing to this assumption, it can be seen that the volume term is insignificant for the FWH formulation on an permeable surface. As mentioned earlier, this is an advantage over the original formulation of the FWH equation for a solid surface, because the costly calculation of the volume integral becomes redundant. Moreover, it should be noted here that a principal advantage of the FWH method over the Kirchhoff method is that the integral surface not necessarily needs to enclose all turbulence. A location closer to the solid walls can be used, which makes the entire CFD computation less costly. However, this increases the error made by neglecting the volume integral term. A solution to Eq. (A.6) can be found, once again, based on Green's function for free space,

$$\begin{aligned} p'_F(\vec{x}, t) = & -\frac{1}{4\pi} \frac{\partial}{\partial x_i} \int_{f=0} \left(\frac{1}{R} [p' \delta_{ij} + \rho u_i u_j]_{\tau} n_j \right) dS \\ & + \frac{1}{4\pi} \frac{\partial}{\partial t} \int_{f=0} \left(\frac{1}{R} [\rho u_i n_j]_{\tau} \right) dS. \end{aligned} \quad (\text{A.7})$$

The above solution to the FWH equation, is the one originally derived for solid surfaces, when neglecting the volume integral. In this formulation, the first and second integral can directly be understood in physical terms as the loading and the thickness noise, respectively [99, 165]. When using a permeable surface, as in the present case, the terms lose their physical meaning and hence it is legitimate to write them as individual integrals as exercised by Yao et al. [93]. In Eq. (A.8), it is then possible to interpret the three terms as the perturbations of pressure, momentum and mass through the surface, respectively.

$$p'_{1,F}(\vec{x}, t) = \frac{1}{4\pi} \int_{f=0} \left(\frac{1}{R} \cos \theta \left[\left\{ \frac{1}{c_0} \frac{\partial}{\partial \tau} + \frac{1}{R} \right\} p' \right]_{\tau} \right) dS, \quad (\text{A.8a})$$

$$p'_{2,F}(\vec{x}, t) = \frac{1}{4\pi} \int_{f=0} \left(\frac{1}{R} \lambda_{ij} \left[\left\{ \frac{1}{c_0} \frac{\partial}{\partial \tau} + \frac{1}{R} \right\} (\rho u_i u_j) \right]_{\tau} \right) dS, \quad (\text{A.8b})$$

$$p'_{3,F}(\vec{x}, t) = \frac{1}{4\pi} \int_{f=0} \left(\frac{1}{R} n_j \left[\frac{\partial}{\partial \tau} (\rho u_j) \right]_{\tau} \right) dS, \quad (\text{A.8c})$$

where $\lambda_{ij} = (r_i/R)n_j$.

A.3 Curle's analogy

Curle's analogy can be regarded as a generalization of Lighthill's analogy [175, 176] in the presence of stationary solid walls. It is possible to derive the Curle equation analogically to Eq. (A.6). Introducing generalized variables into the compressible Navier-Stokes equations

and rewriting them in terms of a wave equation with non-zero source terms, leads to

$$\begin{aligned} \bar{\square}^2 p'(\vec{x}, t) = & -\frac{\partial}{\partial x_i} [p' n_i \delta(f)] \\ & + \frac{\bar{\partial}^2}{\partial x_i x_j} [T_{ij} H(f)]. \end{aligned} \quad (\text{A.9})$$

Obviously, Eq. (A.9) is identical with the FWH equation, if a stationary solid surface is regarded in Eq. (A.6). A stationary, solid surface in the FWH method means that $u_i = u_j = 0$, which makes that Eq. (A.6) directly returns to Eq. (A.9). The solution to the Curle equation is given by the free space Green function as

$$\begin{aligned} p'_C(\vec{x}, t) = & -\frac{1}{4\pi} \frac{\partial}{\partial x_i} \int_{f=0} \left(\frac{1}{R} [p']_{\tau} n_i \right) dS \\ & + \frac{1}{4\pi} \frac{\bar{\partial}^2}{\partial x_i x_j} \int_V \left(\frac{1}{R} [T_{ij}]_{\tau} \right) dV. \end{aligned} \quad (\text{A.10})$$

In Eq. (A.10), the surface integral stands for the pressure fluctuations on the solid wall due to the turbulent boundary layer. The second term represents the impact on the solid surface of the sound waves stemming from the quadrupoles in the flow field. Since only the pressure perturbations are of interest in this study, the volume integral in Eq. (A.10) is disregarded and the total noise for Curle's method can be obtained in the form presented by Yao et al. [92, 93],

$$p'_C(\vec{x}, t) = \frac{1}{4\pi} \int_{f=0} \left(\frac{1}{R} \cos \theta \left[\left\{ \frac{1}{c_0} \frac{\partial}{\partial \tau} + \frac{1}{R} \right\} p' \right]_{\tau} \right) dS. \quad (\text{A.11})$$

Now, it becomes clear that Eq. (A.11) is the same as Eq. (A.8a) in the present formulation of the FWH approach.